AGU PUBLICATIONS

Journal of Advances in Modeling Earth Systems

RESEARCH ARTICLE
10.1002/2016MS000855

**Key Points:**
- A toy model of tropical convection is developed to test the potential utility of a moisture storage closure
- The degree to which moisture convergence accounts for moisture storage is prescribed for two fundamental vertical modes
- Aspects of observations including the moisture-rainfall curve are reproduced with a proper choice of parameters

**Correspondence to:**
H. Masunaga,
masunaga@nagoya-u.jp

**Citation:**
Masunaga, H. and Y. Sumi (2017), A toy model of tropical convection with a moisture storage closure, *J. Adv. Model. Earth Syst.*, *9*, doi:10.1002/2016MS000855.

Received 6 NOV 2016
Accepted 1 MAR 2017
Accepted article online 7 MAR 2017



# A toy model of tropical convection with a moisture storage closure

**Hirohiko Masunaga[1] and Yukari Sumi[2]**

[1]Institute for Space-Earth Environmental Research, Nagoya University, Nagoya, Japan, [2]Graduate School of Environmental Studies, Nagoya University, Nagoya, Japan

**Abstract** A time-dependent, zero-dimensional toy model is constructed to study the large-scale variability in association with tropical moist convection. Case studies from sounding-array observations are analyzed as a benchmark to test the model performance. The model predicts the vertical integral of vertical moisture advection decomposed into the deep convective and congestus/stratiform modes. A closure representing the consumption efficiency of water vapor into precipitation is introduced using the moisture storage ratio, or the degree to which the vertical moisture advection associated with each vertical mode accounts for moisture storage. The observations suggest that this moisture consumption is highly inefficient for the convective/stratiform mode while efficient for the deep convective mode. The model solution is interpreted as a delayed response to the diabatic forcing, unless the sum of the moisture storage ratio and gross moist stability is negative, in which case the system is unstable. Baseline experiments with a fixed moisture storage closure overall reproduce the vertical moisture advection and precipitation as observed, but fail to simulate a sharp pickup of precipitation in the well-known moisture-rainfall curve. This deficiency is eliminated when the moisture storage ratio is allowed to vary as convection intensifies and dissipates.

## 1. Introduction

Raining cumulus clouds such as congesti and cumulonimbi are rooted on a relatively thin subcloud layer, with the cloud base height determined by the lifting condensation level (LCL) being often as low as 500 m over tropical oceans. Given that the water vapor scale height, say ∼2 km, is markedly higher than LCL, low-level convergence brought by a deep overturning circulation would result in an accumulation of moisture above cloud base more than below. This dynamic moisture accumulation is balanced out largely by precipitation in active convective disturbances. The classic parcel model of cumulus clouds, however, does not involve any mechanism to condense out water vapor from the ambient air above cloud base, because moisture is by design supplied only through cloud base. The entrainment of environmental air into clouds would relax this restriction on the nonentraining parcel model, but at the same time the entrainment reduces the in-cloud buoyancy and is unlikely to offer an efficient process promoting convection after all.

Recent satellite data analyses [*Masunaga*, 2013, 2014] showed that while moisture convergence is the main driver of precipitation for highly organized convective systems, precipitation from modest, less organized systems tends to rely largely on local evaporation and subcloud layer moisture convergence in accordance with the parcel model expectation. It is thus speculated that the availability or unavailability of midtropospheric moisture convergence for rainfall may be a critical element in differentiating the nature of tropical convective systems, although the physical processes governing such distinction have yet to be clarified.

The main interests of this work lie in the degree to which moisture convergence is convertible into precipitation and the relevance of this degree to the whole large-scale dynamics involving moist convection. To this end, a simple toy model of tropical convection is developed with a "moisture storage closure" as a prescribed measure of the inefficiency of precipitation production. This approach contrasts with, if not contradicts, conventional parameterizations employed for atmospheric models of different levels of complexity. A large family of models have been built around versions of the convective quasi-equilibrium theory [e.g., *Arakawa and Schubert*, 1974; *Betts*, 1986; *Emanuel et al.*, 1994] (a recent review is given by *Raymond and Herman* [2011]). A quasi-equilibrium postulate makes assumptions principally about the thermal effects of moist convection, so the roles of humidity are not as explicit as those of temperature in the quasi-

equilibrium thinking per se. The relevance of tropospheric water vapor to rainfall, on the other hand, is of central interest for a school of theory of tropical convection. Among the earliest along this line of research is *Raymond* [2000], who derived a conceptual model under the hypothesis that precipitation is inversely proportional to the saturation deficit. A close link between tropospheric humidity and precipitation is a key ingredient in different models of tropical waves (see review by *Sugiyama* [2009]) in the weak temperature gradient (WTG) framework [*Sobel et al*., 2001], where a moisture perturbation is instrumental in controlling the convective variability in lieu of buoyancy anomalies that are promptly smoothed out. An empirical relationship of precipitation (or convective heating) with midtropospheric humidity is explicitly specified in some models of convectively coupled equatorial waves [*Khouider and Majda*, 2006; *Fuchs and Raymond*, 2007; *Kuang*, 2008a].

The present study shares the interests with those studies in which a main focus is put on the link of rainfall with water vapor, but is unique that precipitation is related to the moisture storage, not to the moisture itself. It will be demonstrated that the major characteristics found in observations are reproduced with a moisture storage closure despite the gross simplicity of the model. The reproducible properties include the known relation between precipitation and tropospheric humidity [e.g., *Bretherton et al*., 2004], despite the fact that the present model does not have such a relationship built in as an assumption.

The paper is structured as follows. Observations of tropical atmosphere during the hours of vigorous convection are first examined in light of the large-scale water and thermal budget (section 2). Sounding array measurements analyzed here serve as the test bed of the toy model constructed in section 3. The model results are presented in section 4 and the findings are summarized and discussed in section 5.

## 2. Observations

### 2.1. Data

Variability in the moisture and thermal budget of the tropical atmosphere is first investigated with sounding array data. The observations are carried out during a coordination of the field campaigns of the Cooperative Indian Ocean Experiment on Intraseasonal Variability in the Year of 2011 (CINDY2011), the Dynamics of the Madden-Julian Oscillation (MJO) (DYNAMO), and the Atmospheric Radiation Measurements (ARM) MJO Investigation Experiment (AMIE) [*Yoneyama et al*., 2013]. The sounding-array data analyzed in this study are taken from the DYNAMO array-averaged product (version 3b) provided by *Johnson and Ciesielski* [2013] and see also *Ciesielski et al*. [2014a, 2014b]. This product also contains the array-averaged surface turbulent fluxes from the TropFlux product [*Praveen Kumar et al*., 2012] and the radiative heat profiles from the Clouds and the Earth's Radiant Energy System (CERES) product [*Wielicki et al*., 1996]. The present analysis focuses on the northern sounding array (NSA), a quadrilateral array located just to the north of the equator over the central Indian Ocean. All the array-mean parameters are 3 hourly except for the daily mean TropFlux surface heat fluxes. In the current analysis, the data are moderately smoothed over time by $\pm$6 h running mean, with the exception of radiative heating rate in which the diurnal cycle is filtered out by $\pm$12 h running mean. Note that the diurnal radiative forcing is unlikely to have predominant effects on oceanic convection, given the fact that precipitation over ocean away from coast depends only weakly on local time [e.g., *Imaoka and Spencer*, 2000].

Three different estimates of array-averaged precipitation are provided in the DYNAMO product, namely, Tropical Rainfall Measuring Mission (TRMM) 3B42 version-7 rainfall [*Huffman et al*., 2007] and $Q_1$ and $Q_2$-budget-derived precipitation, $P_s$ and $P_q$, respectively, defined as [*Yanai et al*., 1973],

$$\langle Q_1 \rangle \equiv D_t \langle s \rangle + \langle \omega \partial_p s \rangle = L P_s + S + \langle Q_R \rangle, \tag{1}$$

and

$$\langle Q_2 \rangle \equiv -L\left(D_t \langle q \rangle + \langle \omega \partial_p q \rangle\right) = L(P_q - E), \tag{2}$$

where $D_t \equiv \partial_t + \mathbf{v} \cdot \nabla$ refers to the Lagrangian derivative operator with respect to horizontal flow, $\mathbf{v}$, angle brackets denote the vertical integral from surface to the 100 hPa level, $s$ is dry static energy (DSE), $q$ is vapor mixing ratio, $\omega$ is vertical pressure velocity, $S$ is surface sensible-heat flux, $E$ is surface evaporation flux, $Q_R$ is net radiative heating rate, and $L$ is the specific latent heat of vapor condensation. Note that all these parameters represent the large-scale mean variables (or the sounding-array averages) throughout this paper.

This work adopts $P_s$ as a primary reference for precipitation because $P_q$ is significantly noisier than $P_s$ on subdaily time scales. It is shown in MJO-oriented studies using DYNAMO sounding-array data [*Johnson et al*., 2015; *Ruppert and Johnson*, 2015] that $P_q$ is overall in good agreement with the TRMM 3B42 rainfall, but the same cannot necessarily be said if a heavy temporal smoothing is not applied to $P_q$. High-frequency fluctuations in $P_q$ are likely attributed to the noisiness of the moisture tendency term computed directly from the observed time series, while this difficulty is virtually absent in the $Q_1$ budget owing to the intrinsic homogeneity of free-tropospheric temperature across tropical latitudes. For the same reason, the Lagrangian moisture storage analyzed here is not derived from the humidity time series as observed, but instead is recalculated with $P_s$ substituted in the moisture budget equation,

$$D_t\langle q\rangle = E - P_s - \langle \omega \partial_p q\rangle. \tag{3}$$

Equation (3) has another advantage that moisture storage is derived independently of horizontal moisture advection. The DYNAMO sounding-array estimates of horizontal moisture advection are known to be biased when the intrusion of a localized dry air mass is not properly captured by the sparsely deployed sounding stations [*Hannah et al*., 2016].

As may have been noticed, the Lagrangian tendency is preferentially used rather than the Eulerian in the current formulation. In fact, the choice between the Eulerian and Lagrangian derivatives would not make any practical difference in light of our research interests, since horizontal advection stays small in the moist static energy (MSE) budget for short-term tropical variations [*Inoue and Back*, 2015a]. Given its minor nature, the horizontal advection term is chosen to be left hidden in the Lagrangian derivative rather than dealt with separately as an independent term. The remaining source/sink terms on the right-hand side are reduced to surface evaporation, precipitation, and vertical moisture advection or equivalently moisture divergence, $\langle q\nabla\cdot\mathbf{v}\rangle$, when integrated over height to the depth of the troposphere. *Hannah et al*. [2016] demonstrated the utility of Lagrangian moisture tendency for studying aspects of the atmospheric moisture budget.

Three 72 h sequences captured by the NSA are selected as benchmark cases. Two of the three cases contain vigorous convective events having a precipitation maximum at 0000 UTC 22 October (event 1) and 0300 UTC 27 November (event 2), corresponding to the third and fourth highest peaks, respectively, in the NSA-averaged precipitation record. The top two convective events are not chosen for these cases because $P_s$ largely underestimates the TRMM 3B42 rainfall (not shown) and the fidelity of budget parameters is not confidently assured. The third example sequence (event 3), centered around 1200 UTC 4 December, is devoid of any notable rainfall event in between the second and third MJO episodes identified during the CYNDY2011/DYNAMO/AMIE observational period [*Yoneyama et al*., 2013].

### 2.2. Vertical Mode Decomposition

The toy model developed later is zero-dimensional in space, dealing with vertically integrated atmospheric variables along with surface fluxes. The detailed vertical profiles of atmospheric parameters are therefore outside the scope, while some fundamental aspects of the vertical structure are retained by means of a truncated series of vertical modes. To transform the observations into a comparable format to the model framework, vertical mode decomposition is applied to the temporal-mean NSA sounding using a conventional methodology [*Fulton and Schubert*, 1985; *Haertel and Johnson*, 1998]. The first four eigenmodes of $\omega$ with a rigid-rid boundary condition are shown in Figure 1. The evolution of each mode coefficient is computed by first projecting the horizontal divergence profile onto a series of its eigenmodes at every time step and then converting those profiles into $\omega$ through the mass conservation equation.

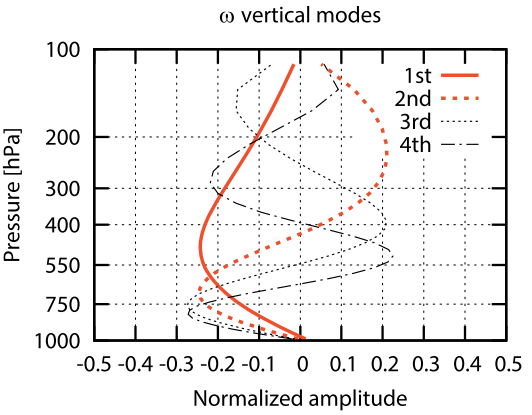


**Figure 1.** The first four eigenmodes of $\omega$ as labeled in the panel with the first and second modes highlighted.

Vertical mode decomposition is known to be of great utility in tropical meteorology in which two or three vertical modes suffice in general to explain

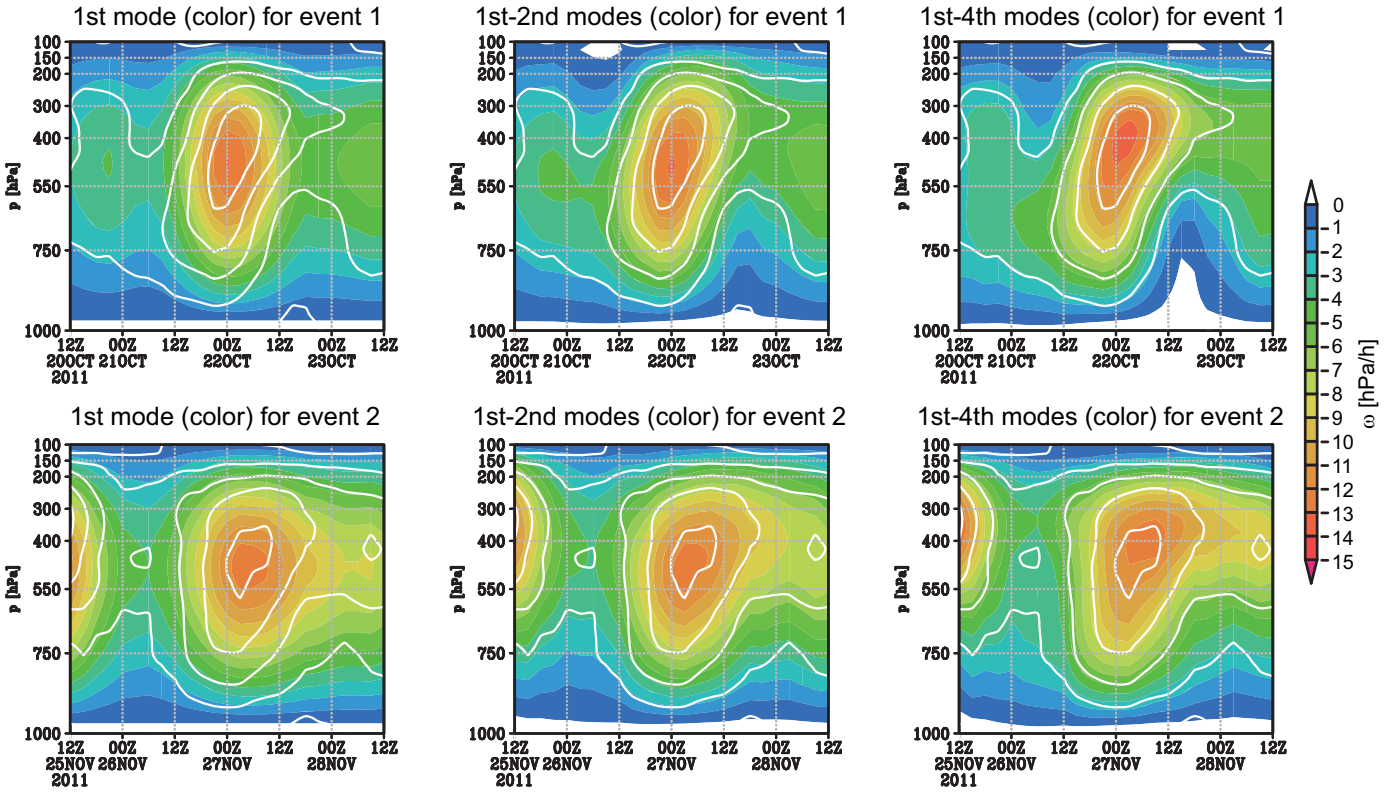


**Figure 2.** Time series of $\omega$ with vertical mode decomposition applied (color shade): the first mode only (left), the first and second modes added together (middle), and the first four modes all combined (right) for event 1 (top) and event 2 (bottom) (see section 2.3 for details of the individual events). The undecomposed $\omega$ is contoured at the interval of 3 hPa $h^{-1}$ in all panels.

the atmospheric dynamics in association with convective heating [*Mapes and Houze*, 1995; *Mapes*, 2000; *Wu et al*., 2000; *Majda and Shefter*, 2001; *Haertel and Kiladis*, 2004; *Khouider and Majda*, 2006; *Back and Bretherton*, 2009]. Figure 2 presented the decomposed $\omega$ profiles for two convective events during DYNAMO that will be examined later in section 2.3. The first eigenmode (color shade in left panels) is responsible for the overall temporal variability of $\omega$ (contoured) but by design fails to explain its vertical tilt. The addition of the second mode (middle panels) improves the reproducibility of the detailed structure of $\omega$ including the tilt. When the third and fourth modes are included as well (right panels), further improvements are visible (e.g., the altitude of the updraft peak for event 1) but the changes are mostly minor. For the sake of convenience, only the first two modes are considered in the analysis to follow. The first eigenmode is hereafter termed as the *deep convective* mode and the second mode as the *congestus/stratiform* mode.

The latter may be simply referred to as the congestus mode when the mode coefficient is positive (i.e., the mode has a low-level updraft) and as the stratiform mode otherwise, following conventional terminology.

### 2.3. Case Studies

Analysis results for event 1 are presented in Figure 3. A sharp precipitation peak is evident (top left panel) in $P_s$ and TRMM 3B42 rainfall. The two precipitation products are in excellent agreement during the hours of active convection in this particular case. The surface evaporation stays consistently small, far short of precipitation especially around its peak intensity. It confirms that moisture convergence should serve as a dominant moisture source of precipitation for intensive convective systems.

The deep convective mode develops in phase with rainfall (top middle panel), with its peak straddled in time by a pair of the congestus/stratiform dipole (bottom middle panel). This is a familiar pattern known to prevail in the tropics over a broad range of time scales [*Mapes et al*., 2006, and references therein], although it is somewhat surprising to find it at this level of clarity in a single convective event. As seen earlier in Figure 2, the deep convective mode dominates the vertical motion in amplitude (note that the color scales are different between the two panels) as also evident in the vertically integrated vertical moisture advection, $-$

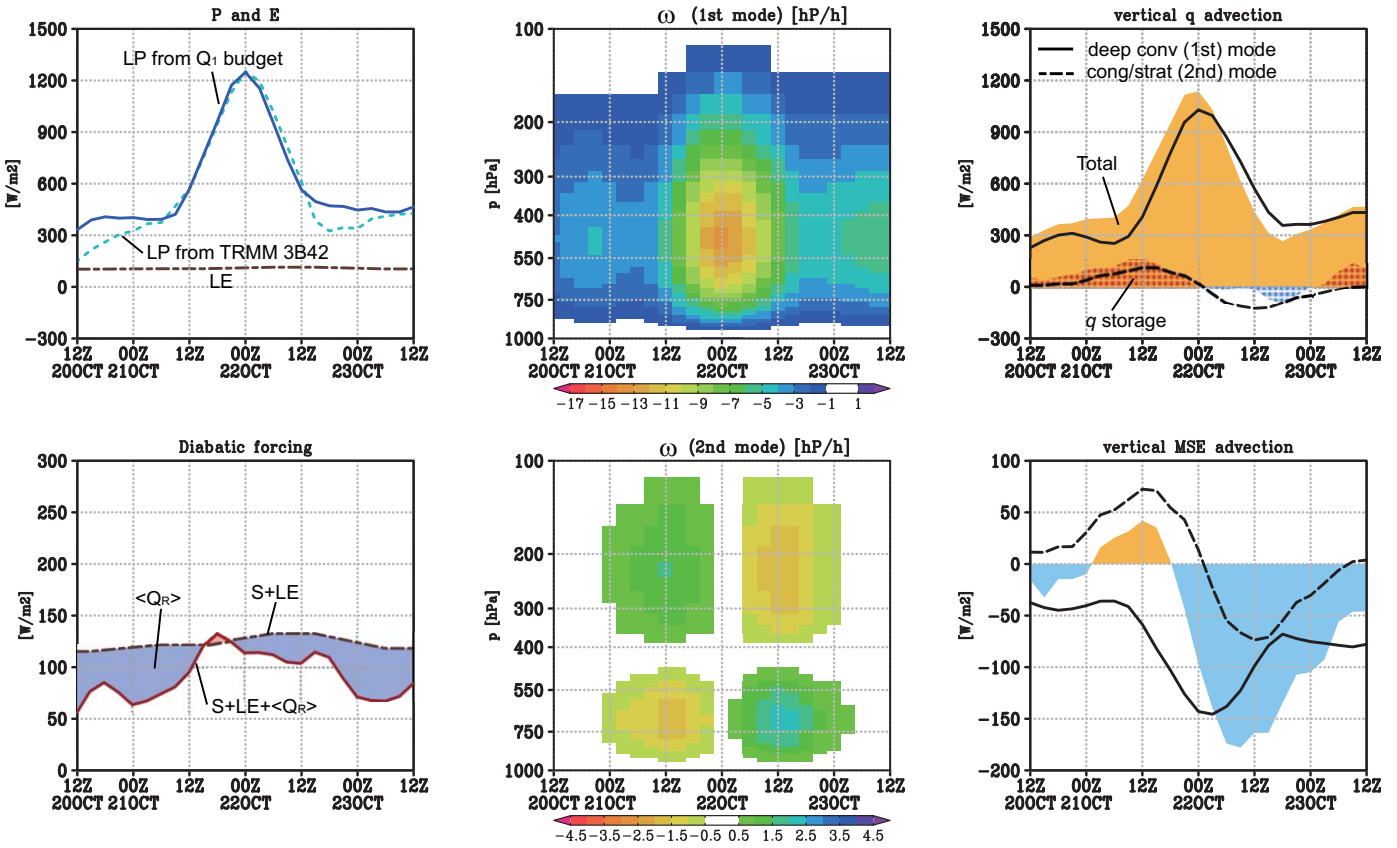


**Figure 3.** Time series of observations for event 1. (top left) $P_s$ (solid), TRMM 3B42 rainfall (dotted), and $E$ (dot-dashed), all in the energy-flux unit (W m$^{-2}$). (Bottom left) Surface heat fluxes or $S + LE$ (dot-dashed), total diabatic forcing or $S+LE+\langle Q_R\rangle$ (solid) with the contribution of $\langle Q_R\rangle$ shaded in red where heating and in blue where cooling (W m$^{-2}$). (top middle) The vertical profile of $\omega$ for the deep convective mode (hPa h$^{-1}$). (bottom middle) The vertical profile of $\omega$ for the congestus/stratiform mode (hPa h$^{-1}$). (top right) $-\langle\omega\partial_p q\rangle$ (shade) with its decomposition into the deep convective mode (solid) and the congestus/stratiform mode (dashed) in the energy-flux unit (W m$^{-2}$). Also plotted in dotted hatch is $\langle D_t q\rangle$ (red where positive and blue where negative). (bottom right) $-\langle\omega\partial_p h\rangle$ (shade), where $h$ denotes moist static energy, with its decomposition into the deep convective mode (solid) and the congestus/stratiform mode (dashed).

$\langle\omega\partial_p q\rangle$ (top right panel). The total $-\langle\omega\partial_p q\rangle$ closely resembles precipitation as expected and is explained to the first approximation by the deep convective mode. The remaining small difference is mostly accounted for by the congestus/stratiform mode, lending confidence in the assumption that these two modes suffice in practice to reproduce the total variability. Interestingly, moisture storage (derived by equation (3)) accords well with the congestus-mode vertical advection, whereas it nearly vanishes after the congestus mode switches to the stratiform mode. The enhancement of the congestus mode accompanying a positive moisture storage results in an import of MSE prior to the peak convection, followed by a rapid buildup of the MSE export associated with the deep convective and stratiform modes as convection dissipates (bottom right panel). The change of MSE in sign from import to export is characteristic of a so-called discharge-recharge model of tropical disturbances [*Peters and Bretherton*, 2006], evidenced also by satellite observations [*Masunaga and L'Ecuyer*, 2014].

All these aspects of the thermodynamic evolution are found also in another case of intensive convection (event 2 in Figure 4). Precipitation, represented in unison by $P_s$ and TRMM 3B42 rainfall, intensifies toward the peak while evaporation remains minor in magnitude (top left panel). The deep convective mode here again evolves in parallel with precipitation (top middle) and is accompanied by the congestus/stratiform mode switching its sign (bottom middle), although the congestus mode is virtually absent and dipole symmetry is not as evident as in event 1. Vertical moisture advection is broken down into the deep convective and congestus/stratiform mode in a similar manner as seen in event 1 (top right), and moisture storage varies coherently with the congestus-mode component of $-\langle\omega\partial_p q\rangle$. Event 2 is likely influenced by a preceding disturbance visible at 1200 UTC 25 November, which might have somewhat distorted the dynamics intrinsic to the disturbance of present interest centered at 0300 UTC 27 November.

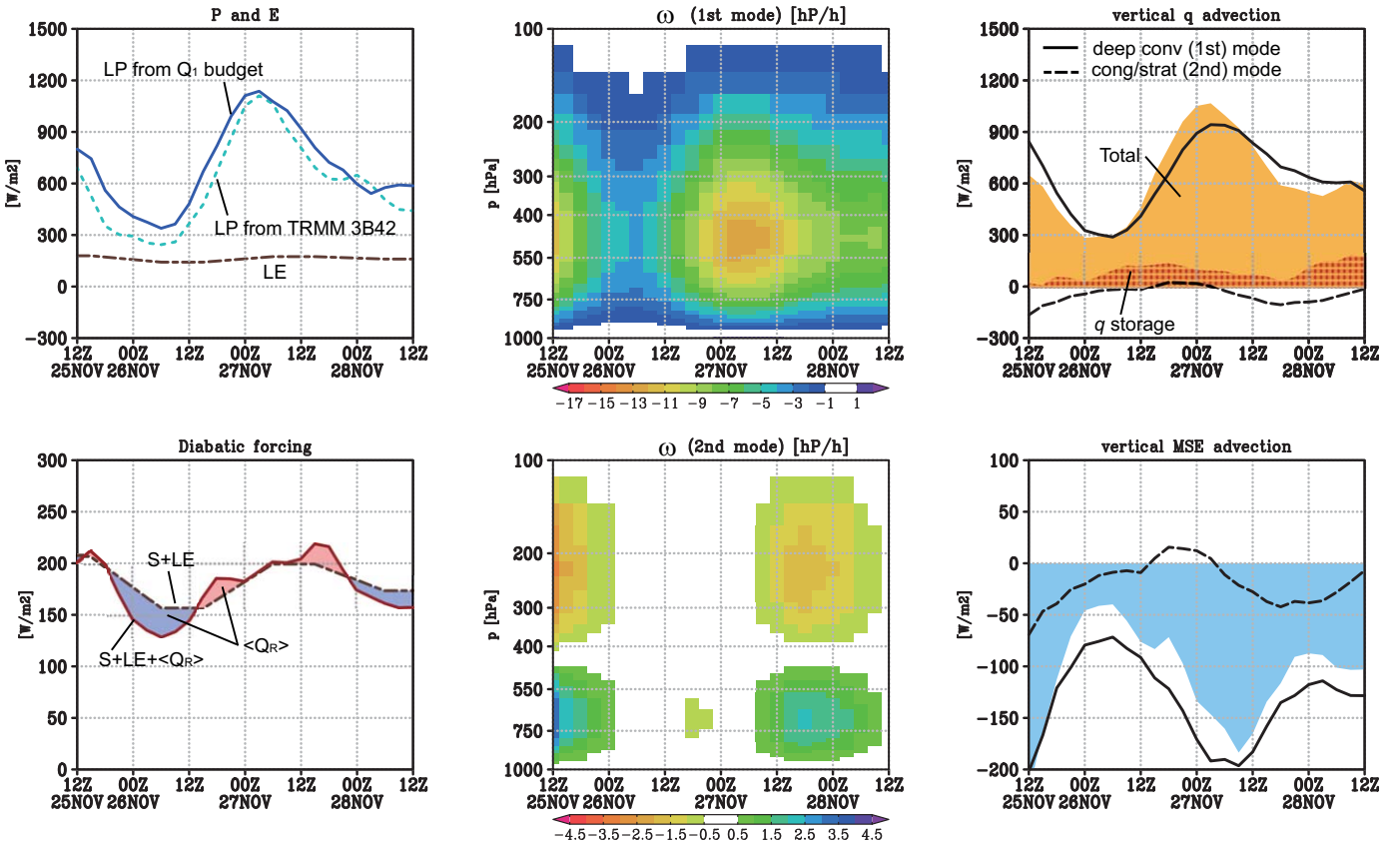


**Figure 4.** Time series of observations for event 2. (top left) $P_s$ (solid), TRMM 3B42 rainfall (dotted), and $E$ (dot-dashed), all in the energy-flux unit (W m$^{-2}$). (bottom left) Surface heat fluxes or $S + LE$ (dot-dashed), total diabatic forcing or $S+LE+\langle Q_R\rangle$ (solid) with the contribution of $\langle Q_R\rangle$ shaded in red where heating and in blue where cooling (W m$^{-2}$). (top middle) The vertical profile of $\omega$ for the deep convective mode (hPa h$^{-1}$). (bottom middle) The vertical profile of $\omega$ for the congestus/stratiform mode (hPa h$^{-1}$). (top right) $-\langle\omega\partial_p q\rangle$ (shade) with its decomposition into the deep convective mode (solid) and the congestus/stratiform mode (dashed) in the energy-flux unit (W m$^{-2}$). Also plotted in dotted hatch is $\langle D_t q\rangle$ (red where positive and blue where negative). (bottom right) $-\langle\omega\partial_p h\rangle$ (shade) with its decomposition into the deep convective mode (solid) and the congestus/stratiform mode (dashed).

Event 3, shown in Figure 5, is a convectively quiescent period. As expected, no notable variation is observed in any parameters studied. The deep convective mode in particular is weaker in amplitude by an order of magnitude, that is, ∼100 W m$^{-2}$ at most in $-\langle\omega\partial_p q\rangle$ for event 3 as opposed to 900 W m$^{-2}$ or larger at the convective peak for events 1 and 2. The difference between the convective and nonconvective events is far less striking in the congestus/stratiform mode and moisture storage, given that their magnitude is as small as ∼100 W m$^{-2}$ regardless of the presence or absence of convection. The close relevance between the congestus-mode component of $-\langle\omega\partial_p q\rangle$ and moisture storage is visible also in event 3 (top right panel), not as evidently as in event 1 but with better clarity than in event 2.

The observations inspire us with a working hypothesis that moisture storage may be ascribed primarily to the congestus-mode component of vertical moisture advection, while its deep-mode counterpart largely precipitates out rather than being accumulated in moisture storage. This idea is mathematically translated as follows in terms of a nondimensional parameter named the *moisture storage ratio*, $\eta$,

$$D_t\langle q\rangle \equiv -\left[\eta_{\rm dc}\langle\omega\partial_p q\rangle_{\rm dc}+\eta_{\rm c/s}\langle\omega\partial_p q\rangle_{\rm c/s}\right], \tag{4}$$

where the subscripts "dc" and "c/s" designate the deep convective mode and the congestus/stratiform mode, respectively. By definition, $\eta_{\rm dc}$ and $\eta_{\rm c/s}$ (or $\eta$ collectively where the general properties of the moisture storage ratio are discussed) are a prescribed measure of the degree to which vertical moisture advection associated with each vertical mode is responsible for moisture storage. The aforementioned hypothesis claims that $\eta_{\rm c/s} \sim 1$ and $\eta_{\rm dc} \sim 0$. The high moisture storage ratio for the congestus mode suggests that the cumulus-cloud types typical of this mode, namely raining shallow cumuli or cumuli congesti, should be highly inefficient in converting the dynamically accumulated moisture into precipitation. The possible

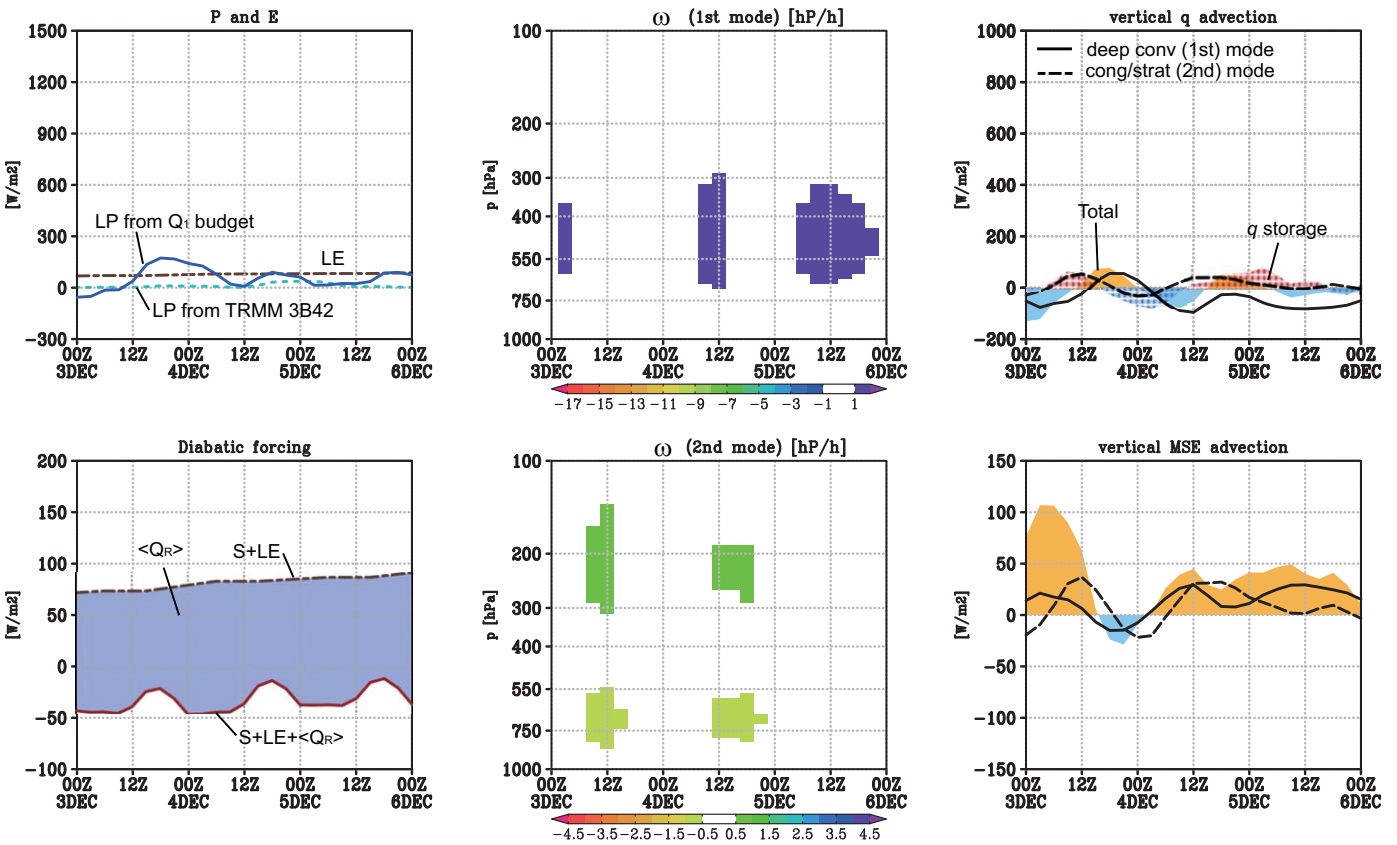


**Figure 5.** Time series of observations for event 3. (top left) $P_s$ (solid), TRMM 3B42 rainfall (dotted), and $E$ (dot-dashed), all in the energy-flux unit (W m$^{-2}$). (bottom left) Surface heat fluxes or $S + LE$ (dot-dashed), total diabatic forcing or $S+LE+\langle Q_R\rangle$ (solid) with the contribution of $\langle Q_R\rangle$ shaded in red where heating and in blue where cooling (W m$^{-2}$). (top middle) The vertical profile of $\omega$ for the deep convective mode (hPa h$^{-1}$). (bottom middle) The vertical profile of $\omega$ for the congestus/stratiform mode (hPa h$^{-1}$). (top right) $-\langle\omega\partial_p q\rangle$ (shade) with its decomposition into the deep convective mode (solid) and the congestus/stratiform mode (dashed) in the energy-flux unit (W m$^{-2}$). Also plotted in dotted hatch is $\langle D_t q\rangle$ (red where positive and blue where negative). (bottom right) $-\langle\omega\partial_p h\rangle$ (shade) with its decomposition into the deep convective mode (solid) and the congestus/stratiform mode (dashed).

reasons behind this include the lack of mechanism for cumulus clouds to effectively condense out midtropospheric moisture as argued in section 1. In contrast, the deep convective mode is considered to involve efficient dynamics for conversion from moisture into precipitation so $\eta_{dc} \sim 0$. The underlying physical processes will be discussed in section 4.4.

The moisture storage term in equation (4) would vanish as integrated over a life cycle of convective disturbances, so that

$$0 = -\left[\eta_{dc}\oint\langle\omega\partial_p q\rangle_{dc}dt + \eta_{c/s}\oint\langle\omega\partial_p q\rangle_{c/s}dt\right], \tag{5}$$

where $\eta_{c/s}$ and $\eta_{dc}$ are assumed to be constant. Figures 3 and 4 suggest that $-\langle\omega\partial_p q\rangle_{dc}$ yields a finite positive value when integrated over time during a convective event, while $-\langle\omega\partial_p q\rangle_{c/s}$ is quasi-sinusoidal and thus would be largely integrated out, that is,

$$-\oint\langle\omega\partial_p q\rangle_{dc}dt > 0,\ -\oint\langle\omega\partial_p q\rangle_{c/s}dt \sim 0. \tag{6}$$

Equations (5) and (6) together offer additional evidence for $\eta_{dc} \sim 0$. Unfortunately, no useful constraint on the possible range of $\eta_{c/s}$ is derived by this line of argument.

It is noted that the formulation itself does not pose any mathematical constraint on the range of $\eta$. From a physical point of view, on the other hand, $\eta_{dc}$ and $\eta_{c/s}$ are unlikely to fall far outside the range between 0 and 1, because $\eta \ll 0$ implies a significant drying that proceeds in spite of dynamic vapor accumulation and $\eta \gg 1$ requires an unusually large evaporation overcompensating the moisture loss due to

precipitation. Such situations, although may temporarily occur in exceptional cases, are in general not typical of tropical convective disturbances and will not be considered in the experiments below.

## 3. Model Design

A toy model is now developed to test the working hypothesis proposed in the previous section. The model is formulated on the basis of the moisture and MSE budget equations,

$$D_t\langle q\rangle = -\left[\langle\omega\partial_p q\rangle_{dc}+\langle\omega\partial_p q\rangle_{c/s}+\langle\omega\partial_p q\rangle_{bg}\right]+E-P, \tag{7}$$

$$D_t\langle h\rangle = -\left[\langle\omega\partial_p h\rangle_{dc}+\langle\omega\partial_p h\rangle_{c/s}+\langle\omega\partial_p h\rangle_{bg}\right]+\Delta F, \tag{8}$$

where $h$ is MSE, $P$ is precipitation, $\Delta F \equiv S+LE+\langle Q_R\rangle$ is the diabatic forcing, and the subscript "bg" denotes the background component that formally represents the unperturbed state unaccounted for by neither the deep convective nor congestus/stratiform mode. Evaporation, precipitation, and the diabatic forcing are also separated into the steady background state and a time-dependent perturbation indicated by prime symbol,

$$E = E_{bg}+E',$$

$$P = P_{bg}+P',$$

$$\Delta F = \Delta F_{bg}+\Delta F'.$$

The background terms are assumed to satisfy the steady state budget equations on their own in the absence of the two convective modes, that is,

$$E_{bg}-P_{bg}-\langle\omega\partial_p q\rangle_{bg}=0, \tag{9}$$

$$\Delta F_{bg}-\langle\omega\partial_p h\rangle_{bg}=0. \tag{10}$$

The background state is factored out by inserting equations (9) and (10) into the budget equations (7) and (8), respectively, leading to

$$D_t\langle q\rangle = -\left[\langle\omega\partial_p q\rangle_{dc}+\langle\omega\partial_p q\rangle_{c/s}\right]+E'-P', \tag{11}$$

$$D_t\langle h\rangle = -\left[\langle\omega\partial_p h\rangle_{dc}+\langle\omega\partial_p h\rangle_{c/s}\right]+\Delta F'. \tag{12}$$

For later reference, an alternative form of the moisture budget equation is derived by substituting equation (4) for the left-hand side of equation (11)

$$-\left[(1-\eta_{dc})\langle\omega\partial_p q\rangle_{dc}+(1-\eta_{c/s})\langle\omega\partial_p q\rangle_{c/s}\right]=P'_{dc}+P'_{c/s}=P', \tag{13}$$

where $P\prime_{dc}$ and $P'_{c/s}$ are the breakdown of precipitation into each vertical mode,

$$P'_{dc}=-(1-\eta_{dc})\langle\omega\partial_p q\rangle_{dc},$$

$$P'_{c/s}=-(1-\eta_{c/s})\langle\omega\partial_p q\rangle_{c/s}. \tag{14}$$

In equation (13), $E'$ has been omitted because the variability of evaporation is practically unimportant compared to $P'$ as shown in Figures 3–5 (top left). It is implied by equations (4) and (14) that vertical moisture advection is partitioned into moisture storage and precipitation by the proportions of $\eta_i$ and $1-\eta_i$, respectively, for each vertical mode represented by the subscript $i$, so precipitation increases with decreasing $\eta_i$ for a given magnitude of $-\langle\omega\partial_p q\rangle_i$.

The MSE budget equation is conveniently rewritten in terms of $q$ rather than $h$. Following a common practice in tropical meteorology, the contribution of DSE is neglected in the MSE tendency term,

$$D_t\langle h\rangle \approx LD_t\langle q\rangle. \tag{15}$$

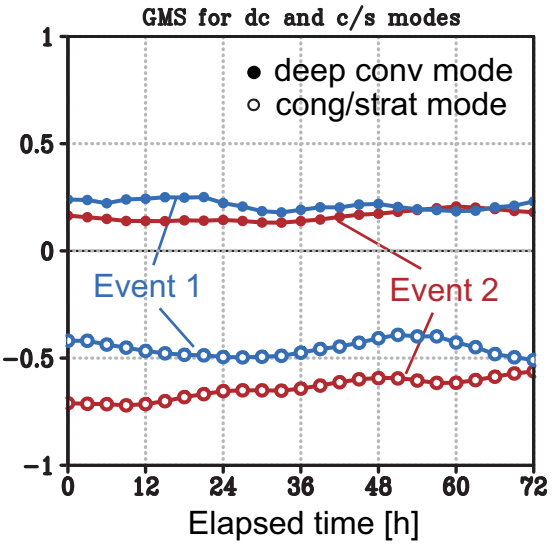


**Figure 6.** Time series of GMS for different vertical modes for event 1 (blue) and event 2 (red). The deep convective mode and the congestus/stratiform mode are indicated by closed and open circles, respectively.

The temperature perturbation, while may not be completely smoothed out on a subdaily time scale, is known to appear in a pair of low-level cooling and upper-level heating during the time of deep convection [e.g., *Mapes and Houze*, 1995] and therefore practically vanishes in the vertical integral [*Masunaga*, 2013].

Vertical MSE advection is replaced by vertical moisture advection in terms of a version of the gross moist stability (GMS) [*Neelin and Held*, 1987],

$$\gamma_{dc} = -\frac{\langle \omega \partial_p h \rangle_{dc}}{L \langle \omega \partial_p q \rangle_{dc}},$$

$$\gamma_{c/s} = -\frac{\langle \omega \partial_p h \rangle_{c/s}}{L \langle \omega \partial_p q \rangle_{c/s}}, \tag{16}$$

where $\gamma_{dc}$ and $\gamma_{dc}$ (or collectively $\gamma$) is defined here individually for each vertical mode in a slightly modified form of the normalized GMS [*Raymond et al.*, 2007, 2009]. GMS for a given vertical eigenmode may be deemed as an externally specified constant when the moisture and DSE profiles are fixed. Figure 6 confirms that GMS for the deep convective mode is almost invariant at 0.2–0.3 in the two convective events studied in section 2.3. GMS remains stable over time when computed for an individual vertical mode owing to the coherence between the numerator and denominator in equation (16), apart from a modest variability due to slight fluctuations in the vertical humidity structure. This stability also holds for the congestus/stratiform mode, whereas the congestus/stratiform mode consistently has a negative GMS, marking a sharp contrast with the deep convective mode.

The fact that the two representative vertical modes have a GMS of opposite signs constitutes an important aspect of the present model as will become clear in section 4.

Equations (12), (15), and (16) are combined into,

$$LD_t\langle q \rangle = L\left[\gamma_{dc}\langle \omega \partial_p q \rangle_{dc} + \gamma_{c/s}\langle \omega \partial_p q \rangle_{c/s}\right] + \Delta F'. \tag{17}$$

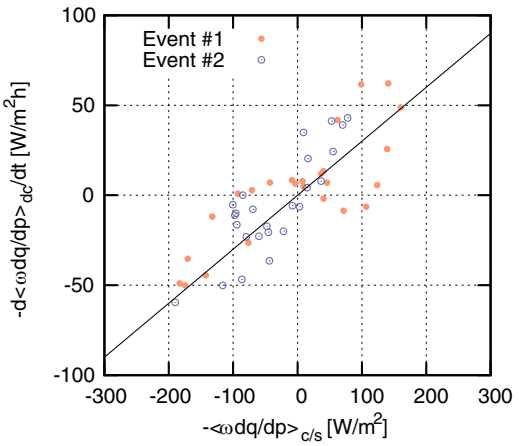


**Figure 7.** Scatterplot of $-\langle \omega \partial_p q \rangle_{c/s}$ (abscissa) versus the time derivative of $-\langle \omega \partial_p q \rangle_{dc}$ (ordinate) from event 1 (closed circles) and event 2 (open circles). A straight line with the inclination of 0.3 $h^{-1}$ is shown as a reference.

Implementing equation (17) with the moisture storage closure (4), one finds a diagnostic equation for vertical moisture advection,

$$-L\left[(\eta_{dc}+\gamma_{dc})\langle \omega \partial_p q \rangle_{dc} + (\eta_{c/s}+\gamma_{c/s})\langle \omega \partial_p q \rangle_{c/s}\right] = \Delta F'. \tag{18}$$

Equation (18) is not closed without an additional assumption relating $-\langle \omega \partial_p q \rangle_{dc}$ and $-\langle \omega \partial_p q \rangle_{c/s}$. An empirical closure is introduced here as,

$$-\frac{d}{dt}\langle \omega \partial_p q \rangle_{dc} = \chi P'_{c/s} = -\chi(1-\eta_{c/s})\langle \omega \partial_p q \rangle_{c/s}, \tag{19}$$

where $\chi$ is a positive constant. Equation (19) is intuitively inspired by the observations in the top right panel of Figures 3 and 4 that $-\langle \omega \partial_p q \rangle_{dc}$ increases with time when $-\langle \omega \partial_p q \rangle_{c/s}$ is positive in sign (the congestus regime) and decreases once it turns to negative (the stratiform regime). This relationship is interpreted implicitly as the convective heating by congestus or

stratiform clouds, $P'_{c/s}$ (see equation (14)), is involved in the growth and dissipation of the deep convective mode. Theoretical arguments relevant to this empirical insight are found in the literature [*Khouider and Majda*, 2006, 2008; *Haertel et al.*, 2008]. Figure 7 shows that the observations clearly verify the positive correlation between $-\langle\omega\partial_p q\rangle_{c/s}$ and the time derivative of $-\langle\omega\partial_p q\rangle_{dc}$ in support of the proportionality claimed by equation (19). Equations (18) and (19) together yield a prognostic equation describing the evolution of $-\langle\omega\partial_p q\rangle_{dc}$,

$$-\tau_* L\frac{d}{dt}\langle\omega\partial_p q\rangle_{dc}=\frac{\Delta F'}{\eta_{dc}+\gamma_{dc}}+L\langle\omega\partial_p q\rangle_{dc}, \tag{20}$$

where

$$\tau_* \equiv \frac{\eta_{c/s}+\gamma_{c/s}}{\chi(1-\eta_{c/s})(\eta_{dc}+\gamma_{dc})}. \tag{21}$$

It is beneficial to first illustrate fundamental aspects of the solution under the simplest condition of a fixed $\Delta F'$. The analytic solution of equation (20) in this special case is

$$-L\langle\omega\partial_p q\rangle_{dc}=-L\langle\omega\partial_p q\rangle_{dc}^{t=0}\exp\left(-\frac{t}{\tau_*}\right)+\frac{\Delta F'}{\eta_{dc}+\gamma_{dc}}\left[1-\exp\left(-\frac{t}{\tau_*}\right)\right]. \tag{22}$$

Equation (22) claims that $-L\langle\omega\partial_p q\rangle_{dc}$ converges toward $\Delta F'/(\eta_{dc}+\gamma_{dc})$ as time proceeds regardless of the initial condition, $-L\langle\omega\partial_p q\rangle_{dc}^{t=0}$, for $\tau_* > 0$. The *e*-folding time scale, $\tau_*$, dictates how quickly this process completes. The solution is analogous to the radiance as a function of optical depth when radiation penetrates through a homogeneously absorbing media, given the mathematical identity between equation (20) and the nonscattering radiative-transfer equation.

The behavior of the solution is entirely different when $\tau_*$ is negative, in which case $-\langle\omega\partial_p q\rangle_{dc}$ would grow exponentially to infinity. Recalling that $0\lesssim\eta\lesssim 1$ and $\gamma_{dc}=$ 0.2–0.3, one can safely expect the denominator in the definition of $\tau_*$ (equation (21)) to be positive definite, with rare exceptions aside. On the other hand, $\eta_{c/s}+\gamma_{c/s}$ in the numerator is only marginally positive or could be even negative because $\gamma_{c/s} < 0$ (Figure 6), implying the possibility that $\tau_*$ could fall to below zero as well. Figure 8 schematically illustrates the evolution of $-\langle\omega\partial_p q\rangle_{dc}$ and $-\langle\omega\partial_p q\rangle_{c/s}$ for two contrasting cases with opposite signs of $\tau_*$. The solution is constrained on a straight line described by equation (18), which is rightward decreasing when $\eta_{c/s}+\gamma_{c/s} > 0$ (or $\tau_* > 0$) and increasing otherwise. Any point laid on the right-half of this plane (i.e., $-\langle\omega\partial_p q\rangle_{c/s} > 0$) proceeds upward along this line while it moves downward if on the left-half of the plane, obeying equation (19). As a consequence, the solution evolves toward the *y* axis until eventually resting on it in cases of $\tau_* > 0$ but moves away from the *y* axis without limit when $\tau_* < 0$. It turns out that the stability of the solution depends on the sign of $\tau_*$.

A brief physical interpretation to this stability criterion may be given as follows. An individual term on the left-hand side of equation (18) is rewritten using $h=s+Lq$ and equations (14) and (16) as

$$-L(\eta_i+\gamma_i)\langle\omega\partial_p q\rangle_i=\langle\omega\partial_p s\rangle_i-LP'_i, \tag{23}$$

where the subscript *i* again represents each vertical mode. In the discussion to follow, $\langle\omega\partial_p q\rangle_i$ is assumed to be negative (i.e., moistening) as is typically the case when convection is developing. It is inferred from equation (23) that diabatic heating $LP'_i$ is short of the work required to drive a large-scale ascent against adiabatic cooling, $\langle\omega\partial_p s\rangle_i$, when $\eta_i+\gamma_i > 0$. This shortage needs to be compensated by the diabatic forcing $\Delta F'$ so that the large-scale ascent is sustained. It follows that the deep convective mode and the congestus/stratiform mode, if both have a positive $\eta_i+\gamma_i$, must compete with each other for a fixed supply of $\Delta F'$, so the system remains stable. The vertical mode with a negative $\eta_i+\gamma_i$, on the contrary, would produce a diabatic heating more than enough to fuel its own vertical motion.

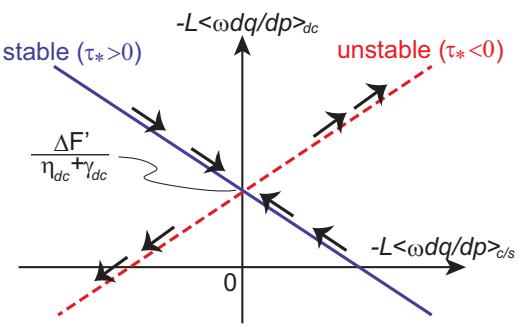


**Figure 8.** Schematic to illustrate the model solution for a constant $\Delta F'$ in terms of $-L\langle\omega\partial_p q\rangle_{dc}$ (ordinate) and $-L\langle\omega\partial_p q\rangle_{c/s}$ (abscissa). See test for details.

If $\eta_{c/s}+\gamma_{c/s}$ is negative, the congestus/stratiform mode gives rise to a residual heating capable of

feeding the deep convective mode as well as itself, enabling a collaborative growth of the two vertical modes. The system therefore could be destabilized once assisted by a positive feedback between the modes as prescribed by equation (19).

A negative $\tau_*$ has the potential to provide a partial explanation for rapidly intensifying convective disturbances in nature, whereas unrealistic without any mechanism to eventually restabilize the system after the instability criterion is met. Such a mechanism is not offered in the current simplistic modeling framework. Throughout the rest of the paper, therefore, $\eta_{c/s}+\gamma_{c/s}$ is restricted to above zero for all model runs.

## 4. Model Results

### 4.1. Experimental Setup

Equation (20) together with the ancillary equation (21) constitutes the core of the current model, delineating the progress in $-\langle\omega\partial_p q\rangle_{dc}$ over time. Its congestus/stratiform counterpart, $-\langle\omega\partial_p q\rangle_{c/s}$, is obtained from the solution using equation (19). Precipitation, $P'$, is then evaluated so the moisture budget equation (13) is satisfied.

Table 1 summarizes the parameter settings for different model runs. The key prescribed parameters characterizing the model are the moisture storage ratios, $\eta_{c/s}$ and $\eta_{dc}$, listed in the first two columns. The default assumptions are $\eta_{c/s}=0.99$ and $\eta_{dc}=0$ as discussed in section 2. Note that $\eta_{c/s}$ is set to be slightly smaller than unity because the right-hand side of equation (19) collapses to zero when $\eta_{c/s}$ is exactly 1. For all experiments except *c/svar* and *fullvar*, $\chi$ (third column) is chosen to satisfy $\chi(1-\eta_{c/s})=0.3\ \mathrm{h}^{-1}$ so that equation (19) best reproduces the observations plotted in Figure 7. Once $\eta_{c/s}$, $\eta_{dc}$, and $\chi$ are given, $\tau_*$ is evaluated with equation (21) as shown in the fifth column. The GMS is fixed for each vertical mode, namely $\gamma_{dc}=0.2$ and $\gamma_{c/s}=-0.5$, for all experiments. Any change to $\gamma_{c/s}$ within a plausible range as expected from Figure 6 does not alter the overall evolution as long as $\eta_{c/s}+\gamma_{c/s}$ stays above zero.

The last column of Table 1 indicates a parameter controlling the variability in diabatic forcing, $v_F$. The diabatic forcing in equation (20) is specified to vary with time as

$$\Delta F' = \frac{\Delta\widehat{F'}}{2}\left[1-\cos\left(2\pi v_F t\right)\right], \tag{24}$$

where $\Delta\widehat{F'}$ is fixed at 150 W m$^{-2}$. Figure 9 (left) depicts equation (24) with three different values of $v_F$ as listed in the top three rows of Table 1. This "cosine-bell" model is aimed at roughly mimicking the observations of diabatic forcing (Figures 3 and 4, bottom left), where the two convective events each exhibit a modest enhancement of $\Delta F'$, driven chiefly by radiative heating for event 1 (Figure 3) and by evaporation for event 2 (Figure 4). Such a systematic variation in the diabatic forcing is not observed for the nonconvective event (Figure 5). Note that $E'$, while ignored in the moisture budget equation, is potentially important for the MSE budget as a part of $\Delta F'$.

### 4.2. Baseline Experiments

First examined are baseline experiments with constant $\eta_{dc}$ and $\eta_{c/s}$. When these parameters are fixed, an analytic solution of equation (20) is derived with the cosine-bell diabatic forcing (24) under the initial condition of $-\langle\omega\partial_p q\rangle_{dc}=0$ as

$$-L\langle\omega\partial_p q\rangle_{dc} = \frac{\Delta\widehat{F'}}{2(\eta_{dc}+\gamma_{dc})\left[1+(2\pi v_F\tau_*)^2\right]}\times \left\{1+(2\pi v_F\tau_*)^2\left[1-\exp\left(-\frac{t}{\tau_*}\right)\right]-\cos\left(2\pi v_F t\right)-2\pi v_F\tau_*\sin\left(2\pi v_F t\right)\right\}, \tag{25}$$

$$-L\langle\omega\partial_p q\rangle_{c/s} = \frac{\pi v_F\Delta\widehat{F'}}{\chi(1-\eta_{c/s})(\eta_{dc}+\gamma_{dc})\left[1+(2\pi v_F\tau_*)^2\right]}\times \left\{2\pi v_F\tau_*\exp\left(-\frac{t}{\tau_*}\right)+\sin\left(2\pi v_F t\right)-2\pi v_F\tau_*\cos\left(2\pi v_F t\right)\right\}. \tag{26}$$

Exponential terms in equations (25) and (26) are ill-defined when $\tau_*$ equals zero. In this special case, the solution may be directly derived from equations (18) and (19) with $\eta_{c/s}+\gamma_{c/s}=0$,

**Table 1.** Experimental Setups. For All Runs, $\gamma_{dc}=0.2$ and $\gamma_{c/s}=-0.5$

| Experiments | $\eta_{c/s}$ | $\eta_{dc}$ | $\chi$ ($h^{-1}$) | $\tau_*$ (h) | $v_F^{-1}$ (h) |
|---|---|---|---|---|---|
| *v24* | | | | | 24 |
| *v48* | 0.99 | 0 | 30 | 8.17 | 48 |
| *cntrl* | | | | | 72 |
| *c/s0.5* | 0.50 | 0 | 0.60 | 0 | |
| *dc0.5* | 0.99 | 0.5 | 30 | 2.33 | |
| *dc0.05* | 0.99 | 0.05 | 30 | 6.53 | 72 |
| *c/svar* | Equation (30) | 0 | 3 | Variable | |
| *fullvar* | Equation (30) | Equation (31) | 3 | Variable | |

$$-L\langle\omega\partial_p q\rangle_{dc}=\frac{\Delta\widehat{F'}}{2(\eta_{dc}+\gamma_{dc})}[1-\cos(2\pi v_F t)], \tag{27}$$

$$-L\langle\omega\partial_p q\rangle_{c/s}=\frac{\pi v_F\Delta\widehat{F'}}{\chi(1-\eta_{c/s})(\eta_{dc}+\gamma_{dc})}\sin(2\pi v_F t). \tag{28}$$

As plotted in Figure 9 (right), the solutions are qualitatively reminiscent of the observations shown in Figures 3 and 4 (top right). Recalling the earlier discussion in the case of a constant $\Delta F'$ (Figure 8), one would expect that $-L\langle\omega\partial_p q\rangle_{dc}$ approaches $\Delta F'/(\eta_{dc}+\gamma_{dc})$ over a finite time of $\tau_*$ as implied by equation (22). As such, the behavior of $-\langle\omega\partial_p q\rangle_{dc}$ may be interpreted as a delayed response to the slowly varying diabatic forcing. The delay would be minimal when $\tau_* \ll v_F^{-1}$, whereas it would become increasingly difficult to keep up with a change of diabatic forcing as $v_F^{-1}$ decreases toward $\tau_*$. This gives an explanation to the differences among the three runs shown in Figure 9. The run with the fastest varying $\Delta F'$ (*v24*) has a small amplitude and an incomplete cycle of $-\langle\omega\partial_p q\rangle$ compared to the others, because the system is not allowed a sufficient time to respond to the forcing. The evolution is otherwise self-similar across a range of $v_F$. The observed undulation of the diabatic forcing has a cycle of roughly one wavelength (Figure 3) or 1.5 wavelengths (Figure 4) over a 72 h period, suggesting that 48–72 h is a realistic choice for $v_F^{-1}$. All the experiments to follow will be run with $v_F^{-1}=72$ h.

The sensitivity of model results to $\eta_{c/s}$ and $\eta_{dc}$ is next investigated. Figure 10 compares the control run ($\eta_{c/s}=0.99$) (left column) and another run with a reduced $\eta_{c/s}$ (*c/s0.5*, right column). The two experiments are nearly identical to each other except for a minor difference in the delay time in the atmospheric response to diabatic forcing. The peak of $-\langle\omega\partial_p q\rangle_{dc}$ occurs at 42 h or slightly later for the control, while located at 36 h in experiment *c/s0.5*. Experiment *c/s0.5* corresponds to the case with $\tau_*=0$, where the delay is absent as indicated by equation (27). Precipitation evolves closely following vertical moisture advection, but with a further delay due to a finite moisture storage (equation (13)). Moisture storage for experiment *c/s0.5* is by design as half in amplitude as $-\langle\omega\partial_p q\rangle_{c/s}$.

Additional runs are carried out where $\eta_{dc}$ is modified instead of $\eta_{c/s}$. Figure 11 (left) shows that an increase of $\eta_{dc}$ from 0 to 0.5 leads to a significant decrease of amplitude. This is explained by the term $\Delta\widehat{F'}/(\eta_{dc}+\gamma_{dc})$ in equations (25) and (26). The sum of $\eta_{dc}$ and $\gamma_{dc}$ scales the strength of convective disturbances for a given diabatic forcing (see Figure 8), as GMS does in its original definition. A positive $\eta_{dc}$ effectively enhances the GMS and hence reduces the amplitude of vertical moisture advection and precipitation. Moisture storage now remains positive over an extended period of time because the first term dominates the second in the right-hand side of equation (4). The evolution more resembles the control experiment when $\eta_{dc}$ is chosen to be a more modest value of 0.05 (Figure 11, right).

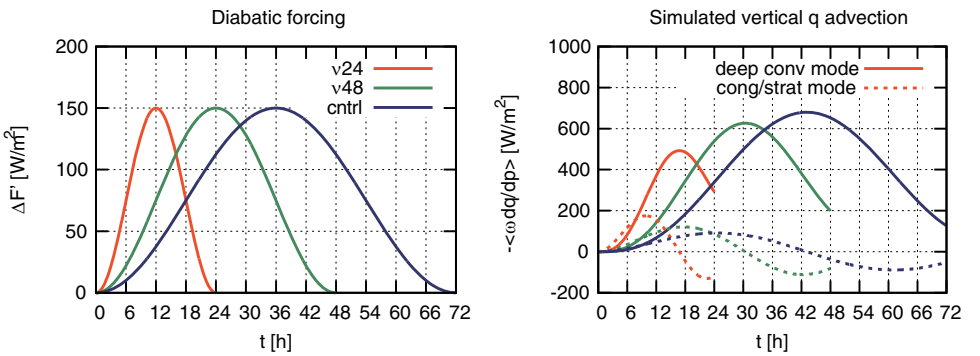


**Figure 9.** (left) $\Delta F'$ as a function of time for $v_F^{-1}=24$ h (experiments *v24*), 48 h (*v48*), and 72 h (*cntrl*). (right) The solutions of $-\langle\omega\partial_p q\rangle_{dc}$ (solid) and $-\langle\omega\partial_p q\rangle_{c/s}$ (dotted) for the three runs.

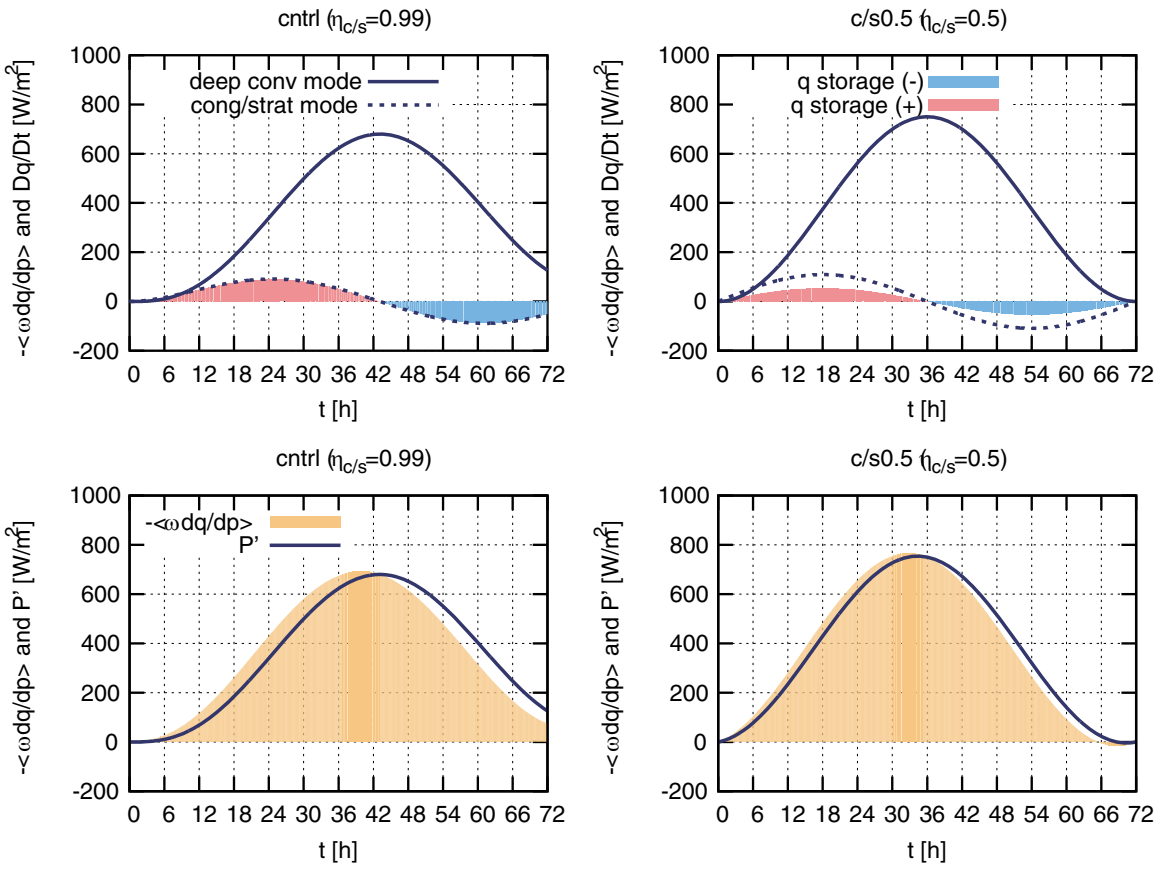


**Figure 10.** (top row) $-\langle\omega\partial_p q\rangle_{dc}$ (solid), $-\langle\omega\partial_p q\rangle_{c/s}$ (dotted), and $D_t\langle q\rangle$ (shaded in red where positive and in blue where negative). (bottom row) Total $-\langle\omega\partial_p q\rangle$ (shaded) and $P\prime$ (solid). (left column) Experiment *cntrl*. (right column) Experiment *c/s0.5*.

### 4.3. Moisture-Precipitation Relation

The current model provides column water vapor (CWV) by integrating equation (17) over time,

$$\langle q'\rangle = \int D_t\langle q\rangle dt = \int \left\{ \left[ \gamma_{dc}\langle\omega\partial_p q\rangle_{dc} + \gamma_{c/s}\langle\omega\partial_p q\rangle_{c/s} \right] + \frac{\Delta F'}{L} \right\} dt, \tag{29}$$

where $\langle q'\rangle$ is the perturbation of CWV to its background state. This quantity, when compared to $P'$ from equation (13), yields the model-predicted relation of CWV with precipitation. Precipitation is known to grow increasingly as the ambient air moistens in the satellite-based climatology [*Bretherton et al.*, 2004; *Peters and Neelin*, 2006] as well as from in situ observations of short-term variability [*Holloway and Neelin*, 2010]. Similarly, an abrupt intensification of precipitation is confirmed once CWV exceeds 60 mm in the sounding array data analyzed here (Figure 12). The CWV-precipitation relationship is assessed as an additional benchmark to test the model against observations.

The results are plotted in Figure 13 for different baseline experiments examined above. Simulated tracks of the CWV-precipitation relationship are found to vary sensitively depending on the choice of $\eta_{c/s}$ and $\eta_{dc}$. Unfortunately, however, all the runs fail to reproduce the rapid pickup of precipitation as expected from the observations. Precipitation is almost linearly correlated with CWV in some runs (*cntrl* and *c/s0.5*), and the rate of rainfall pickup saturates rather than grows further as CWV becomes larger for other runs (*dc0.5* and *dc0.05*). All the trajectories make a clockwise turn, as opposed to the satellite observations composited in the context of the convective life cycle [*Masunaga*, 2012]. A thorough parameter search (not shown) has proven that this apparent deficiency is not mitigated by merely tuning $\eta_{c/s}$ or $\eta_{dc}$ to another fixed value.

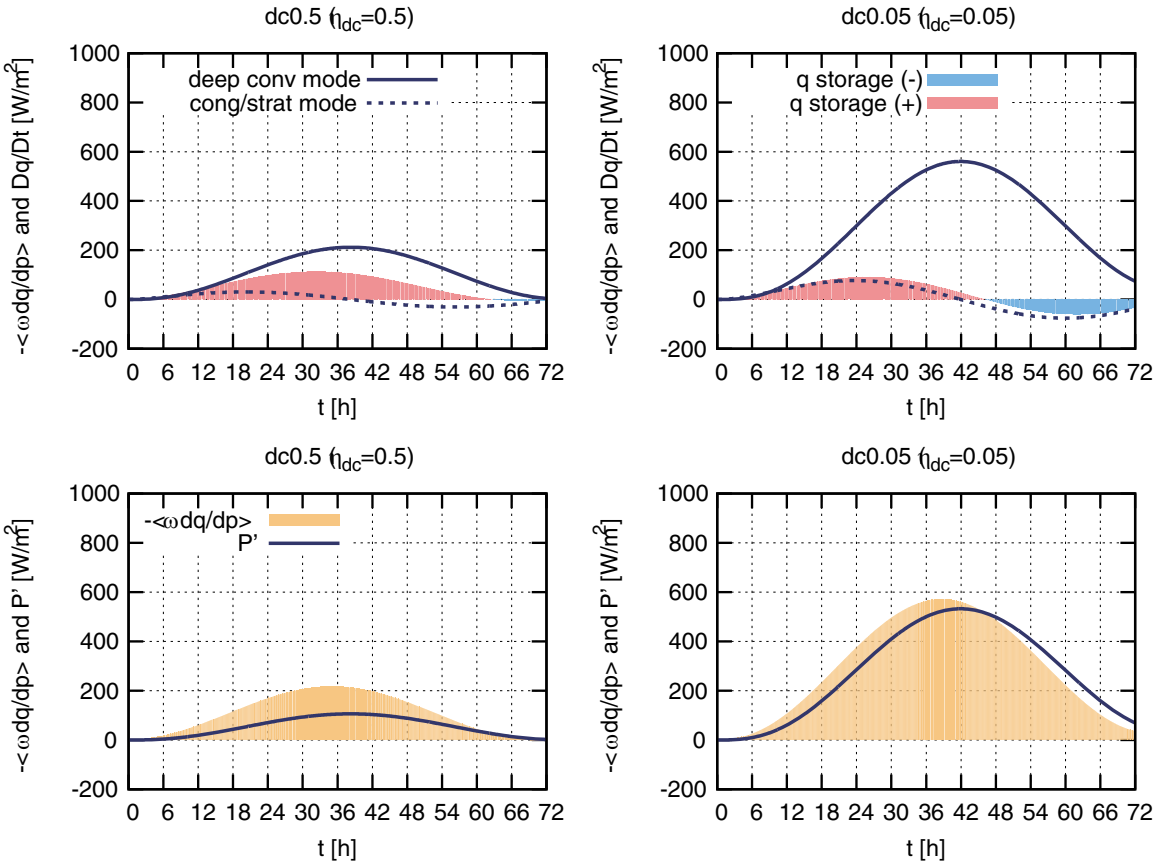


**Figure 11.** (top row) $-\langle\omega\partial_p q\rangle_{dc}$ (solid), $-\langle\omega\partial_p q\rangle_{c/s}$ (dotted), and $D_t\langle q\rangle$ (shaded in red where positive and in blue where negative). (bottom row) Total $-\langle\omega\partial_p q\rangle$ (shaded) and $P'$ (solid). (left column) Experiment dc0.5. (right column) Experiment dc0.05.

### 4.4. Experiments With Variable $\eta$

The moisture storage ratio, $\eta$, is assumed to be invariant in the model runs shown so far. This restriction limits the flexibility in the conversion efficiency from vertical moisture advection to precipitation and is presumably one of the reasons why the model is incapable of reproducing the increasingly intensifying rainfall as CWV increases (Figure 13). The assumption of constant $\eta$ is relaxed in two experiments to follow so that $\eta_{c/s}$ and $\eta_{dc}$ are each variable according to a prescribed function (defined below).

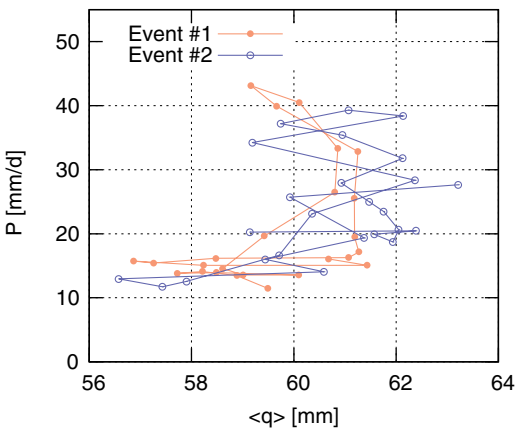


**Figure 12.** The evolutionary track of the observations in the CWV-precipitation plane for events 1 (filled circles) and 2 (open circles) (see section 2 for the definition). Adjacent points on each line are 3 h apart.

It was argued in sections 1 and 2.3 that cumulus convection lacks an efficient mechanism to condense out moisture in the ambient air above cloud base, offering a possible explanation for $\eta_{c/s} \sim 1$ as suggested from the observations. There is, on the other hand, a potential pathway for midtropospheric moisture to precipitate out through cumulus dynamics. Since the large-scale mean cloud mass flux at cloud base is balanced out to a large degree by subsidence mass flux from above at the same height [e.g., *Yanai et al.*, 1973, Figure 13], an appreciable portion of the subcloud-layer moisture fed into convective clouds can be in theory traced back to the downward moisture flux from the midtroposphere. While a dry subsidence into the subcloud layer in general would work against the

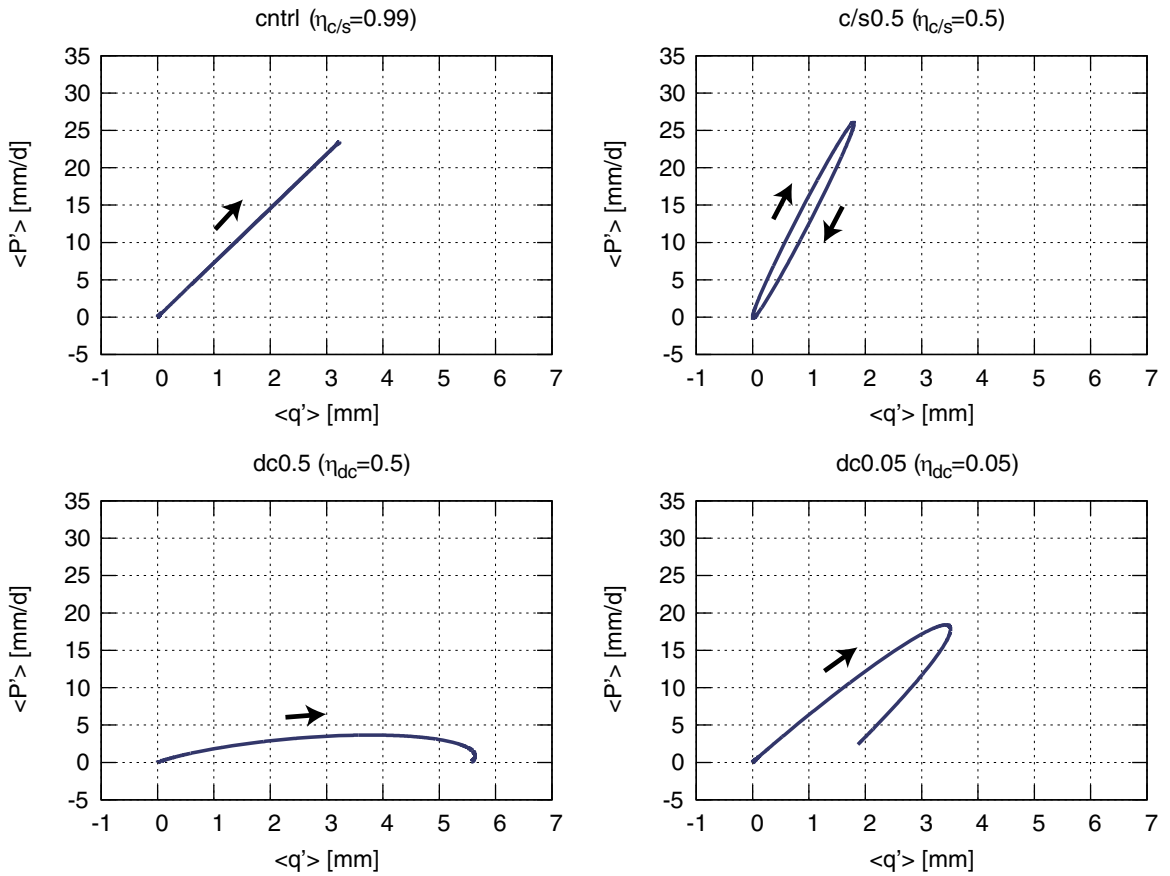


**Figure 13.** Simulated tracks of the CWV-precipitation relationship in terms of $\langle q\prime \rangle$ (abscissa) and $P\prime$ (ordinate) for four baseline experiments. Arrows indicate the evolutionary direction along the track. (left top) *cntrl*, (right top) *c/s0.5*, (left bottom) *dc0.5*, and (right bottom) *dc0.05*.

maintenance of moist convection, a strong convective downdraft could mechanically force further convection once cold pools develop. *Risi et al*. [2008] found by use of stable water isotopes that the proportion of unsaturated downdraft in the subcloud-layer moisture budget amounts to 34% for light precipitation and 45% for strong precipitation, the latter of which in particular is comparable to the contribution of environmental subsidence of 43–45%. It is therefore hypothesized that convective downdrafts, once developed to a certain degree, could intensify themselves without being diluted anymore by environmental subsidence, pulling down more and more midtropospheric moisture that is then fed into subsequent cumuli. This process, if occurring fast enough at a subhourly time scale typical of cumulus processes compared to the large-scale variability taking place over daily time scales as seen in Figures 3 and 4, would be regarded virtually as an instantaneous condensation of midtropospheric water vapor from the moisture budget perspectives.

A modification to $\eta_{c/s}$ to mimic this effect is made in a rather heuristic manner,

$$\eta_{c/s}=\eta_{0,c/s}\left(1-\frac{P'}{\Pi_{c/s}}\right), \tag{30}$$

where $\eta_{0,c/s}$=0.99 and $L\Pi_{c/s}$=4000 W m$^{-2}$. The choice of $\Pi_{c/s}$ here is arbitrary but must be large enough to satisfy $P'/\Pi_{c/s} \ll 1$, because otherwise $\eta_{c/s}$ could decrease across the stability criterion of $\eta_{c/s}+\gamma_{c/s}=0$. Equation (30) embodies a primitive expectation that an increase in $P'$ would reinforce convective downdrafts with cold pools and hence feedback on precipitation through equation (14). Given the lack of any theory that analytically formulates $\eta$ in terms of precipitation, $\eta_{c/s}$ is related linearly with $P'$ with all higher-order terms left out of consideration for the sake of brevity.

Equation (20) combined with equation (30) is integrated numerically with other parameters being equal to the control setup in experiment *c/svar* (Figure 14, left). Although $\eta_{c/s}$ changes only mildly from 0.99 to about

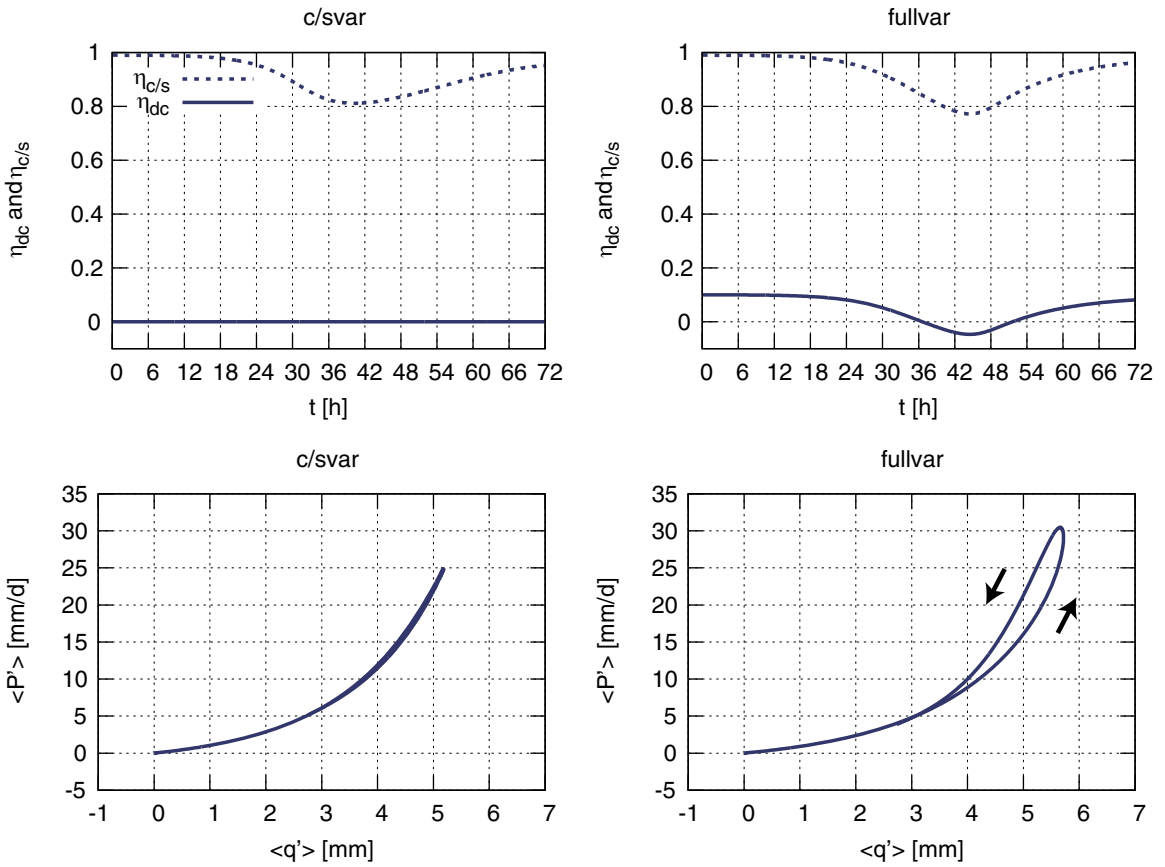


**Figure 14.** (top row) $\eta_{c/s}$ and $\eta_{dc}$ as a function of time. (bottom row) Simulated tracks of the CWV-precipitation relationship in terms of $\langle q\prime \rangle$ (abscissa) and $P\prime$ (ordinate). Arrows indicate the evolutionary direction along the track. (left column) Experiment *c/svar*. (right column) Experiment *fullvar*.

0.8 then back toward 1, the evolutionary track in the CWV-precipitation plane has improved significantly compared to the baseline experiments (Figure 13). Precipitation now grows increasingly with CWV toward its higher end as often found in the literature [*Bretherton et al*., 2004; *Raymond et al*., 2007; *Holloway and Neelin*, 2010].

The hypothetical process of feeding cumuli with midtropospheric moisture by way of the subcloud layer would be further facilitated in the presence of the deep convective mode, as deep convection likely generates considerably stronger downdrafts than congesti. This may explain why $\eta_{dc}$ is closer to 0 rather than 1 in the first place, but yet it is somewhat extreme that $\eta_{dc}$ is fixed at zero all the time. To relax this assumption, $\eta_{dc}$ is also perturbed in a similar manner to $\eta_{c/s}$ (but within a range close to zero) as

$$\eta_{dc}=\eta_{0,dc}\left(1-\frac{P'}{\Pi_{dc}}\right), \tag{31}$$

where $\eta_{0,dc}=0.1$ and $L\Pi_{dc}=600$ W m$^{-2}$ (Experiment *fullvar*). The shape of the trajectory remains similar to experiment *c/svar*, but the rising and returning branches of the trajectory are now split apart (Figure 14, right). Such a counter-clockwise turn in the CWV-precipitation curve is as found in the observations by *Masunaga* [2012]. The magnitude of the variability is about 6 mm for $\langle q' \rangle$ and 30 mm/d for $P'$, which compares well with the observations plotted in Figure 12.

Vertical moisture advection and precipitation simulated in experiments *c/svar* and *fullvar* are shown in Figure 15. Unlike the striking differences in the CWV-precipitation curve, the evolution of vertical moisture advection and precipitation is overall reminiscent of the previous experiments (Figures 10 and 11). It is evident, however, that the new runs with variable $\eta$, especially the *fullvar* run, exhibit a sharper rise of precipitation toward the peak than the baseline experiments. The new runs turn out to be better in line with the observations in which the precipitation peak width is narrow compared to the modestly undulating diabatic

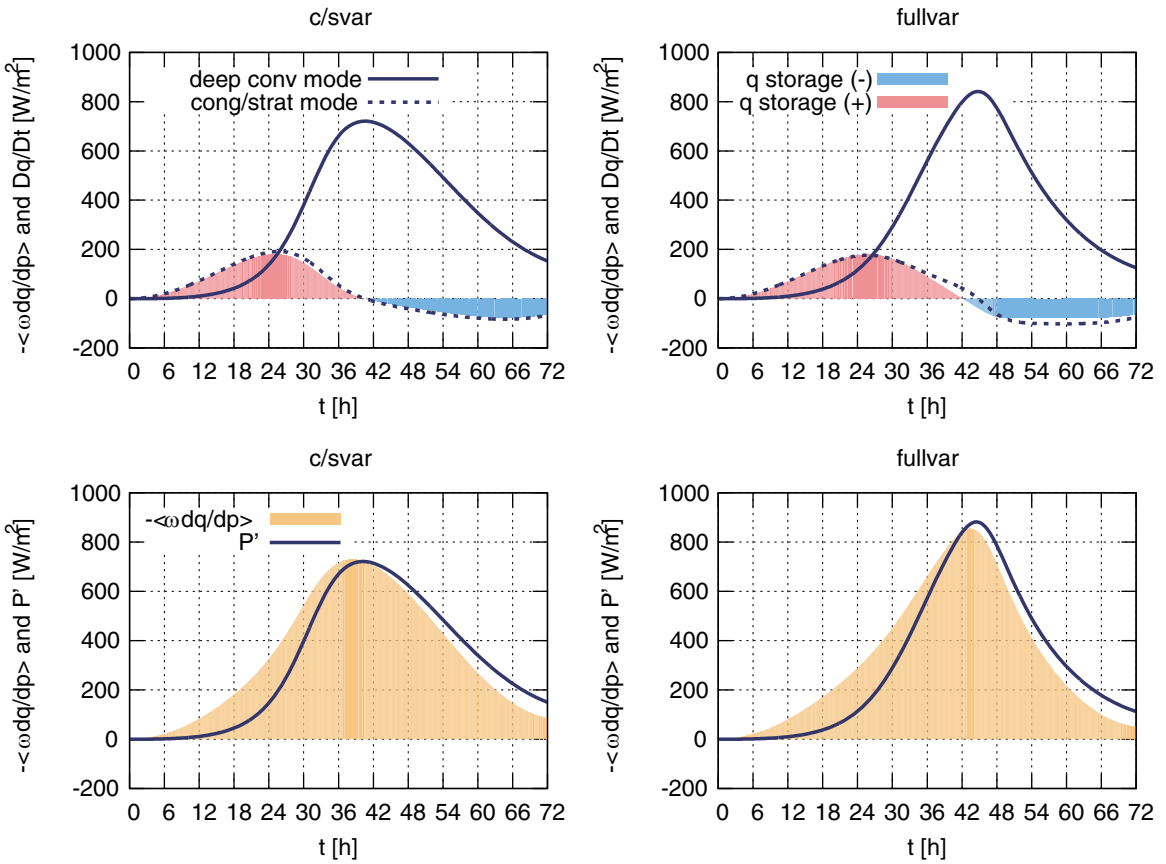


**Figure 15.** (top row) $-\langle\omega\partial_p q\rangle_{dc}$ (solid), $-\langle\omega\partial_p q\rangle_{c/s}$ (dotted), and $D_t\langle q\rangle$ (shaded in red where positive and in blue where negative). (bottom row) Total $-\langle\omega\partial_p q\rangle$ (shaded) and *PI* (solid). (left column) Experiment *c/svar*. (right column) Experiment *fullvar*.

forcing (Figures 3 and 4). An additional sanity test for those runs is performed with the simulated tracks projected onto Figure 7, where the second closure assumption (19) is checked for validity. Figure 16 confirms that the experiments *c/svar* and *fullvar* stay within a range consistent with the observations.

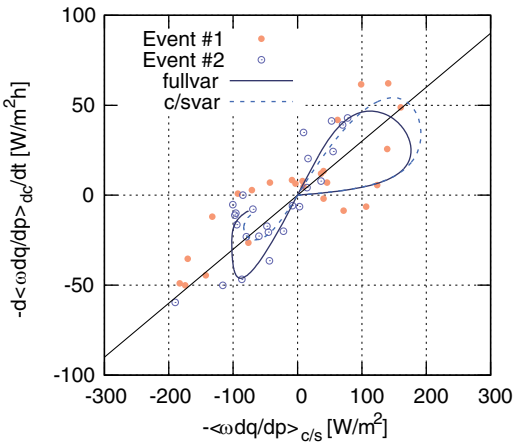


**Figure 16.** Scatterplot of $-\langle\omega\partial_p q\rangle_{c/s}$ (abscissa) versus the time derivative of $-\langle\omega\partial_p q\rangle_{dc}$ (ordinate) from event 1 (closed circles) and event 2 (open circles). A straight line with the inclination of 0.3 $h^{-1}$ is shown as a reference. Simulated tracks from the *c/svar* and *fullvar* experiments are overlaid.

## 5. Conclusion and Discussion

The large-scale dynamics associated with tropical moist convection was studied using sounding array observations and a time-dependent, zero-dimensional model. The model predicts the vertical integral of vertical moisture advection (or equivalently of moisture divergence) with a vertical mode decomposition applied into the deep convective and congestus/stratiform modes, denoted by $-\langle\omega\partial_p q\rangle_{dc}$ and $-\langle\omega\partial_p q\rangle_{c/s}$, respectively. The variability in vertical moisture advection is a proxy of the intensity of large-scale updraft since the temperature and humidity profiles do not change drastically over a time scale of interest (subdaily to a few days). Each vertical mode is assigned the moisture storage ratio, $\eta_{dc}$ and $\eta_{c/s}$ defined in equation (4), as a measure of the fraction of vertical moisture advection is left unconsumed without being

immediately precipitated out. Case studies from the CINDY2011/DYNAMO/AMIE sounding array data were examined as an observational benchmark to test the model fidelity. The observations suggest that $\eta_{c/s}$ is on the order of unity, inferring that congestus clouds do not involve an efficient mechanism to produce rainfall despite a column moistening by vertical moisture advection. This does not contradict the naive expectation that the efficiency of cumulus precipitation would be limited because a significant portion of moisture convergence takes place above cloud base in the humid tropical atmosphere. As such, $\eta$ may be regarded as a parameter representing the nature of cumulus convection and thus serves as a closure dealing with unresolved processes for the large-scale dynamics.

A second closure relation is introduced by equation (19) to empirically characterize the connection between the two vertical modes, where the deep convective mode is parameterized to grow or decline depending on the sign of the congestus/stratiform mode as evidenced by the observations. The resulting prognostic equation (20) together with an ancillary parameter $\tau_*$ summarizing the closure assumptions (equation (21)) founds the basis for the model. The solution indicates that $-\langle\omega\partial_p q\rangle_{dc}$ behaves as a delayed response to the diabatic forcing $\Delta F'$ with an *e*-folding time given by $\tau_*$ when $\tau_* \geq 0$. The magnitude of $-\langle\omega\partial_p q\rangle_{dc}$ is approximated well by $\Delta F'/(\eta_{dc}+\gamma_{dc})$ if the diabatic forcing changes slowly compared to $\tau_*$ as is usually the case (see Table 1). The observations suggest that $\eta_{dc}$ stays small near zero and $\gamma_{dc}$ is 0.2–0.3, and therefore the diabatic forcing is amplified by a factor of 3–5 in $-\langle\omega\partial_p q\rangle_{dc}$. The value of $\gamma_{dc}$ may be closer to zero in an environment where the midtropospheric moisture is more abundant than the present sounding over the Indian Ocean. The updraft could be much stronger for a given diabatic forcing in such an environment.

If $\tau_*$ is negative, the system becomes unstable as $-\langle\omega\partial_p q\rangle_{dc}$ diverges to infinity. The stability criteria on $\tau_*$ is in practice controlled by the sign of $\eta_{c/s}+\gamma_{c/s}$, where $\gamma_{c/s}$ refers to the GMS associated with the congestus/stratiform mode. Under general circumstances $\eta_{c/s}+\gamma_{c/s}$ is a small positive number and the system is stable, although the possibility of a negative $\eta_{c/s}+\gamma_{c/s}$ is not ruled out since $\gamma_{c/s} < 0$ by nature.

A negative GMS would in theory cause a thermodynamic instability [*Raymond*, 2000; *Raymond et al*., 2009] and could explain a self-sustaining growth of the system in numerical simulations of tropical convection [*Bretherton et al*., 2005; *Sessions et al*., 2010]. The condition for instability is $\gamma_{c/s}+\eta_{c/s} < 0$ instead of $\gamma_{c/s} < 0$ in the present formulation, so that a negative GMS per se would not give rise to an instability unless $\gamma_{c/s}$ further decreases to below $-\eta_{c/s}$. In this regard, $\eta_{c/s}$ acts as a moderator to GMS that relaxes, to a certain degree, the stability criterion as previously documented. This role of $\eta_{c/s}$ might be instrumental for interpreting negative values of GMS in nature, which are observed without invoking violent instability where a bottom-heavy circulation climatologically prevails as is typical of the tropical eastern Pacific [*Back and Bretherton*, 2006]. As discussed above, however, the possibility remains that an instability could take place when $\eta_{c/s}+\gamma_{c/s}$ reduces to a negative value, since no absolute physical constraint seems to exist against it. We do not pursue this issue in this work.

GMS for different vertical modes, by definition, does not add up to the value calculated with all the modes combined first into the vertical advection terms. The latter definition of GMS changes rapidly as convection develops and dissipates [*Sessions et al*., 2010; *Masunaga and L'Ecuyer*, 2014; *Inoue and Back*, 2015b], while $\gamma_{dc}$ and $\gamma_{c/s}$ are each less variable by design, especially in sign. The quasi-constant nature of the mode-specific GMS is an important element of the present model.

The simulations for an externally specified diabatic forcing as a cosine-bell function of time qualitatively capture the observed variation in $-\langle\omega\partial_p q\rangle_{dc}$ and $-\langle\omega\partial_p q\rangle_{c/s}$ (Figures 10 and 11). In baseline experiments with fixed $\eta_{dc}$ and $\eta_{c/s}$, the evolution of $-\langle\omega\partial_p q\rangle_{dc}$ is, as expected, an amplified response to the cosine-bell $\Delta F'$ with a slight temporal delay. This appears to infer that moist convection only mirrors the external forcing with little internal freedom to drive its own dynamics, which is obviously at odds with the conventional wisdom in mesoscale meteorology. This deficiency is mitigated to a reasonable extent by allowing $\eta_{dc}$ and $\eta_{c/s}$ to vary with time, giving a flexibility to the model so it can somehow handle the dynamics inherent in convective systems. Two of the model runs were carried out with a heuristic assumption relating $\eta$ with precipitation in attempt to take into account a positive feedback on precipitation at the intensifying stage of convective systems. The precipitation peak is sharpened in these runs as actually observed in contrast with an overly broad peak simulated in the baseline experiment.

The CWV-precipitation relationship offers another useful test bed for the model. The steep rise in precipitation with the environmental moistening as well known in the literature is not reproducible when $\eta_{dc}$ and $\eta_{c/s}$ are fixed. Runs with variable $\eta_{dc}$ and $\eta_{c/s}$, on the other hand, are successful in simulating major properties of the observations in the CWV-precipitation curve. It may be worth stressing that the known CWV-

precipitation curve is able to be reproduced by a simplistic conceptual model in a prognostic way, given that a consensus has not been reached in the physical reasoning behind it [*Raymond and Zeng*, 2005; *Muller et al*., 2009; *Neelin et al*., 2009; *Raymond et al*., 2009; *Yano et al*., 2012]. The current model predicts the CWV-precipitation curve as a trajectory tracing the life cycle of convective systems, where changes of $\eta$ in the course of the evolution play a crucial role in controlling the trajectory morphology. The evolution begins with a nearly horizontal path in the CWV-precipitation plane because of a positive moisture storage with minimal precipitation (i.e., $\eta \sim 1$), while the path makes a quick turn into a vertical stretch as $\eta$ reduces. Note that the CWV-precipitation curve here is identical in shape for any initial condition (or any background state) with no reference to the absolute values of CWV and precipitation. This finding is consistent with the satellite data analysis by *Masunaga* [2012], in which a family of self-similar evolutionary tracks emerges regardless of column relative humidity (CRH) in the environment. The universality in the climatological CRH-precipitation relationship [*Bretherton et al*., 2004] therefore does not apply as is on an instantaneous basis, but is explicable only as the statistical ensemble of many different tracks each representing the individual life cycle of convection [*Masunaga*, 2012; *Ahmed and Schumacher*, 2015].

The moisture storage closure (equation (4)) relates precipitation to the moisture tendency instead of moisture itself. The sharp rainfall pickup in the present model is thus not a manifestation of the moisture control on rainfall, but results from the increasing efficiency of precipitation production as convection intensifies. Although a moist environment would be arguably more favorable for intense convection than a drier one, parameterizing precipitation (or convective heating) in terms of midtropospheric humidity, as done for example in an explicit manner by *Raymond* [2000], may not necessarily be a fully appropriate strategy in light of causality.

Equations (14) and (19) together lead to

$$\frac{d}{dt}\frac{P'_{\mathrm{dc}}}{1-\eta_{\mathrm{dc}}} = \chi P'_{\mathrm{c/s}}, \tag{32}$$

implying that $P'_{\mathrm{dc}}$ is in quadrature with $P'_{\mathrm{c/s}}$, with a minor deviation when $\eta_{\mathrm{dc}}$ changes with time. In the present model, therefore, the stratiform heating delays behind the deep convective heating by a fixed phase lag ($\sim$90°) rather than by a fixed time lag, unlike the early work on the stratiform instability assuming a constant lag of $\sim$3 h [e.g., *Mapes*, 2000; *Majda and Shefter*, 2001]. The constant time lag was questioned by *Kuang* [2008b], based on his finding that the time lag enhances linearly with an increasing wavelength of simulated waves. The present model is in line with *Kuang* [2008b] in this aspect.

The diabatic forcing is considered as strictly external to the model in the present paper, although the model formulation readily allows to connect the diabatic forcing with the model outputs if desired. This is a possible future update to the model, as is to incorporate the potential impacts of the radiative-convective feedbacks and wind-induced surface heat exchange (WISHE).

The model formulation satisfies the thermal and moisture budget equations while relying on multiple tunable assumptions in need of further refinement. While the observations narrow down the plausible ranges of $\eta_{\mathrm{dc}}$ and $\eta_{\mathrm{c/s}}$, robust theoretical reasoning for this parameterization has yet to be sought. By definition, $\eta_{\mathrm{dc}}$ and $\eta_{\mathrm{c/s}}$ are related to the conversion efficiency of moisture convergence into precipitation through cumulus-scale processes associated with each vertical mode. A potentially useful strategy to quantify this efficiency may be analyzing cloud-resolving model (CRM) runs forced by specified large-scale dynamics. Equations (30) and (31), or the dependence of $\eta$ on precipitation for the *c/svar* and *fullvar* runs, are highly ad hoc and should be updated as well with more sophisticated physics.

The current zero-dimensional model as a whole is obviously limited in practical utility, but a moisture storage closure as examined in this paper would be worth testing with a full-dimensional model capable of simulating realistic convective disturbances.

**Acknowledgments**
The authors thank Johnny Luo, Kuni Inoue, and an anonymous reviewer for their valuable comments and helpful suggestions. The CINDY2011/DYNAMO/AMIE sounding array data set was produced by Dick Johnson and Paul Ciesielsky and is distributed at http://johnson.atmos.colostate.edu/dynamo/products/array_averages/. This work was supported by the Japan Society for the Promotion of Science (JSPS) grant-in-aid (KAKENHI) for Scientific Research (B) (26287113) and Challenging Exploratory Research (26610150).

## References

Ahmed, F., and C. Schumacher (2015), Convective and stratiform components of the precipitation-moisture relationship, *Geophys. Res. Lett.*, *42*, 10,453–10,462, doi:10.1002/2015GL066957.

Arakawa, A., and W. H. Schubert (1974), Interaction of a cumulus cloud ensemble with the large-scale environment: Part I, *J. Atmos. Sci.*, *31*, 674–701.

Back, L. E., and C. S. Bretherton (2006), Geographic variability in the export of moist static energy and vertical motion profiles in the tropical Pacific, *Geophys. Res. Lett.*, *33*, L17810, doi:10.1029/2006GL026672.
Back, L. E., and C. S. Bretherton (2009), A simple model of climatological rainfall and vertical motion patterns over the tropical oceans, *J. Clim.*, *22*, 6477–6497, doi:10.1175/2009JCLI2393.1.
Betts, A. K. (1986), A new convective adjustment scheme. Part I: Observational and theoretical basis, *Q. J. R. Meteorol. Soc.*, *112*, 677–691.
Bretherton, C. S., M. E. Peters, and L. E. Back (2004), Relationships between water vapor path and precipitation over the tropical oceans, *J. Clim.*, *17*, 1517–1528.
Bretherton, C. S., P. N. Blossey, and M. Khairoutdinov (2005), An energy-balance analysis of deep convective self-aggregation above uniform SST, *J. Atmos. Sci.*, *62*, 4273–4292.
Ciesielski, P. E., R. H. Johnson, K. Yoneyama, and R. K. Taft (2014a), Mitigation of Sri Lanka island effects in Colombo sounding data and its impact on DYNAMO analyses, *J. Meteorol. Soc. Jpn.*, *92*, 385–405.
Ciesielski, P. E., R. H. J. H. Yu, K. Yoneyama, M. Katsumata, C. N. Long, J. Wang, S. M. Loehrer, K. Young, S. F. Williams, W. Brown, J. Braun, and T. van Hove (2014b), Quality-controlled upper-air sounding dataset for DYNAMO/CINDY/AMIE: Development and corrections, *J. Atmos. Oceanic Technol.*, *31*, 741–764.
Emanuel, K. A., J. D. Neelin, and C. S. Bretherton (1994), On large-scale circulations in convecting atmospheres, *Q. J. R. Meteorol. Soc.*, *120*, 1111–1143.
Fuchs, Ž., and D. J. Raymond (2007), A simple, vertically resolved model of tropical disturbances with a humidity closure, *Tellus Ser. A*, *59*, 344–354.
Fulton, S. R., and W. H. Schubert (1985), Vertical normal mode transforms: Theory and application, *Mon. Weather Rev.*, *113*, 647–658.
Haertel, P. T., and R. H. Johnson (1998), Two-day disturbances in the equatorial western Pacific, *Q. J. R. Meteorol. Soc.*, *124*, 615–636.
Haertel, P. T., and G. N. Kiladis (2004), Dynamics of 2-day equatorial waves, *J. Atmos. Sci.*, *61*, 2707–2721.
Haertel, P. T., G. N. Kiladis, A. Denno, and T. M. Rickenbach (2008), Vertical-mode decompositions of 2-day waves and the Madden-Julian Oscillation, *J. Atmos. Sci.*, *65*, 813–833.
Hannah, W. M., B. E. Mapes, and G. S. Elsaesser (2016), A Lagrangian view of moisture dynamics during DYNAMO, *J. Atmos. Sci.*, *73*, 1967–1985.
Holloway, C. E., and J. D. Neelin (2010), Temporal relations of column water vapor and tropical precipitation, *J. Atmos. Sci.*, *67*, 1091–1105.
Huffman, G. J., R. F. Adler, D. T. Bolvin, G. Gu, E. J. Nelkin, K. P. Bowman, Y. Hong, E. F. Stocker, and D. B. Wolff (2007), The TRMM multi-satellite precipitation analysis: Quasi-global, multi-year, combined-sensor precipitation estimates at fine scale, *J. Hydrometeorol.*, *8*, 38–55.
Imaoka, K., and R. W. Spencer (2000), Diurnal variation of precipitation over the tropical oceans observed by TRMM/TMI combined with SSM/I, *J. Clim.*, *13*, 4149–4158.
Inoue, K., and L. E. Back (2015a), Column-integrated moist static energy budget analysis on various time scales during TOGA COARE, *J. Atmos. Sci.*, *72*, 1856–1870.
Inoue, K., and L. E. Back (2015b), Gross moist stability assessment during TOGA COARE: Various interpretations of gross moist stability, *J. Atmos. Sci.*, *72*, 4148–4166.
Johnson, R. H., and P. E. Ciesielski (2013), Structure and properties of Madden-Julian Oscillations deduced from DYNAMO sounding arrays, *J. Atmos. Sci.*, *70*, 3157–3179.
Johnson, R. H., P. E. Ciesielski, J. H. Ruppert Jr., and M. Katsumata (2015), Sounding-based thermodynamic budgets for DYNAMO, *J. Atmos. Sci.*, *72*, 598–622.
Khouider, B., and A. J. Majda (2006), A simple multicloud parameterization for convectively coupled tropical waves: Part I: Linear analysis, *J. Atmos. Sci.*, *63*, 1308–1323.
Khouider, B., and A. J. Majda (2008), Multicloud models for organized tropical convection: Enhanced congestus heating, *J. Atmos. Sci.*, *65*, 895–914.
Kuang, Z. (2008a), A moisture-stratiform instability for convectively coupled waves, *J. Atmos. Sci.*, *65*, 834–854.
Kuang, Z. (2008b), Modeling the interaction between cumulus convection and linear gravity waves using a limited-domain cloud system-resolving model, *J. Atmos. Sci.*, *65*, 576–591.
Majda, A. J., and M. G. Shefter (2001), Models for stratiform instability and convectively coupled waves, *J. Atmos. Sci.*, *58*, 1567–1584.
Mapes, B. (2000), Convective inhibition, subgrid-scale triggering energy, and stratiform instability in a toy tropical wave model, *J. Atmos. Sci.*, *57*, 1515–1535.
Mapes, B., S. Tulich, J. Lin, and P. Zuidema (2006), The mesoscale convection life cycle: Building block or prototype for large-scale tropical waves?, *Dyn. Atmos. Oceans*, *42*, 3–29.
Mapes, B. E., and R. A. Houze Jr. (1995), Diabatic divergence profiles in western Pacific mesoscale convective systems, *J. Atmos. Sci.*, *52*, 1807–1828.
Masunaga, H. (2012), Short-term versus climatological relationship between precipitation and tropospheric humidity, *J. Climate*, *25*, 7983–7990.
Masunaga, H. (2013), A satellite study of tropical moist convection and environmental variability: A moisture and thermal budget analysis, *J. Atmos. Sci.*, *70*, 2443–2466.
Masunaga, H. (2014), Free-tropospheric moisture convergence and tropical convective regimes, *Geophys. Res. Lett.*, *41*, 8611–8618, doi: 10.1002/2014GL062301.
Masunaga, H., and T. S. L'Ecuyer (2014), A mechanism of tropical convection inferred from observed variability in the moist static energy budget, *J. Atmos. Sci.*, *71*, 3747–3766.
Muller, C. J., L. E. Back, P. A. O'Gorman, and K. A. Emanuel (2009), A model for the relationship between tropical precipitation and column water vapor, *Geophys. Res. Lett.*, *36*, L16804, doi:10.1029/2009GL039667.
Neelin, J. D., and I. M. Held (1987), Modeling tropical convergence based on the moist static energy budget, *Mon. Weather Rev.*, *115*, 3–12.
Neelin, J. D., O. Peters, and K. Hales (2009), The transition to strong convection, *J. Atmos. Sci.*, *66*, 2367–2384.
Peters, M. E., and C. S. Bretherton (2006), Structure of tropical variability from a vertical mode perspective, *Theor. Comput. Fluid Dyn.*, *20*, 501–524, doi:10.1007/s00162-006-0034-x.
Peters, O., and J. D. Neelin (2006), Critical phenomena in atmospheric precipitation, *Nat. Phys.*, *2*, 393–396, doi:10.1038/nphys314.
Praveen Kumar, B., J. Vialard, M. Lengaigne, V. S. N. Murt, and M. J. McPhaden (2012), Tropflux: Air-sea fluxes for the global tropical oceans—Description and evaluation, *Clim. Dyn.*, *38*, 1521–1543, doi:10.1007/s00382-011-1115-0.
Raymond, D. J. (2000), Thermodynamic control on tropical rainfall, *Q. J. R. Meteorol. Soc.*, *126*, 889–898.

Raymond, D. J., and M. J. Herman (2011), Convective quasi-equilibrium reconsidered, *J. Adv. Model. Earth Syst.*, *3*, M08003, doi:10.1029/2011MS000079.

Raymond, D. J., and X. Zeng (2005), Modelling tropical atmospheric convection in the context of the weak temperature gradient approximation, *Q. J. R. Meteorol. Soc.*, *131*, 1301–1320.

Raymond, D. J., S. L. Sessions, and Ž. Fuchs (2007), A theory for the spinup of tropical depressions, *Q. J. R. Meteorol. Soc.*, *133*, 1743–1754.

Raymond, D. J., S. L. Sessions, A. H. Sobel, and Ž. Fuchs (2009), The mechanics of gross moist stability, *J. Adv. Model. Earth Syst.*, *1*, 9, doi:10.3894/JAMES.2009.1.9.

Risi, C., S. Bony, and F. Vimeux (2008), Influence of convective processes on the isotopic composition ($\delta^{18}$O and $\delta$D) of precipitation and water vapor in the tropics: 2. Physical interpretation of the amount effect, *J. Geophys. Res.*, *113*, D19306, doi:10.1029/2008JD009943.

Ruppert, J. H., Jr., and R. H. Johnson (2015), Diurnally modulated cumulus moistening in the preonset stage of the Madden-Julian Oscillation during DYNAMO, *J. Atmos. Sci.*, *72*, 1622–1646.

Sessions, S. L., S. Sugaya, D. J. Raymond, and A. H. Sobel (2010), Multiple equilibria in a cloud]resolving model using the weak temperature gradient approximation, *J. Geophys. Res.*, *115*, D12110, doi:10.1029/2009JD013376.

Sobel, A. H., J. Nilsson, and N. L. Polvani (2001), The weak temperature gradient approximation and balanced tropical moisture waves, *J. Atmos. Sci.*, *58*, 3650–3665.

Sugiyama, M. (2009), The moisture mode in the quasi-equilibrium tropical circulation model. part I: Analysis based on the weak temperature gradient approximation, *J. Atmos. Sci.*, *66*, 1507–1523.

Wielicki, B. A., B. R. Barkstrom, E. F. Harrison, R. B. Lee III, G. L. Smith, and J. E. Cooper (1996), Clouds and the Earth's Radiant Energy System (CERES): An Earth Observing System experiment, *Bull. Am. Meteorol. Soc.*, *77*, 853–868.

Wu, Z., E. S. Sarachik, and D. S. Battisti (2000), Vertical structure of convective heating and the three-dimensional structure of the forced circulation on an equatorial beta plane, *J. Atmos. Sci.*, *57*, 2169–2187.

Yanai, M., S. Esbensen, and J.-H. Chu (1973), Determination of bulk properties of tropical cloud clusters from large scale heat and moisture budgets, *J. Atmos. Sci.*, *30*, 611–627.

Yano, J.-I., C. Liu, and M. W. Moncrieff (2012), Self-organized criticality and homeostasis in atmospheric convective organization, *J. Atmos. Sci.*, *69*, 3449–3462.

Yoneyama, K., C. Zhang, and C. N. Long (2013), Tracking pulses of the Madden-Julian Oscillation, *Bull. Am. Meteorol. Soc.*, *94*, 1871–1891.